Utilisation of probabilistic MT inversions to constrain magnetic data inversion: proof-of-concept and field application

Jérémie Giraud[1,2,3*], Hoël Seillé[4], Mark D. Lindsay[1,5,6], Gerhard Visser[4], Vitaliy Ogarko[1,2], Mark W. Jessell[1,2].

[1] Centre for Exploration Targeting (School of Earth Sciences), University of Western Australia, 35 Stirling Highway, Crawley, Australia.
[2] Mineral Exploration Cooperative Research Centre, School of Earth Sciences, University of Western Australia, 35 Stirling Highway, WA Crawley 6009 Australia.
[3] GeoRessources, Université de Lorraine, Rue du doyen Marcel Roubault, Vandoeuvre-lès-Nancy, France.
[4] Commonwealth Scientific and Industrial Research Organisation, Deep Earth Imaging Future Science Platform, Australian Resources Research Centre, Kensington, Australia.
[5] Commonwealth Scientific and Industrial Research Organisation, Mineral Resources, Australian Resources Research Centre, Kensington, Australia.
[6] ARC Industrial Transformation Training Centre in Data Analytics for Resources and Environment (DARE)
[*]now at GeoRessources, Université de Lorraine, Rue du doyen Marcel Roubault, Vandoeuvre-lès-Nancy, France.

Correspondence to: Jeremie Giraud (jeremie.giraud@uwa.edu.au)

Abstract. We propose, test and apply a methodology integrating 1D magnetotelluric (MT) and magnetic data inversion, with a focus on the characterization of the cover-basement interface. It consists of a cooperative inversion workflow relying on standalone inversion codes. Probabilistic information about the presence of rock units is derived from MT and passed on to magnetic inversion through constraints combining such structural constraints with petrophysical prior information. First, we perform the 1D probabilistic inversion of MT data for all sites and recover the respective probabilities of observing the cover-basement interface, which we interpolate to the rest of the study area. We then calculate the probabilities of observing the different rock units and partition the model into domains defined by combinations of rock units with non-zero probabilities. Third, we combine such domains with petrophysical information to apply spatially-varying, disjoint interval bound constraints to least-squares magnetic data inversion. We demonstrate the proof-of-concept using a realistic synthetic model reproducing features from the Mansfield area (Victoria, Australia) using a series of uncertainty indicators. We then apply the workflow to field data from the prospective mining region of Cloncurry (Queensland, Australia). Results indicate that our integration methodology efficiently leverages the complementarity between separate MT and magnetic data modelling approaches and can improve our capability to image the cover-basement interface. In the field application case, our findings also suggest that the proposed workflow may be useful to refine existing geological interpretations and to infer lateral variations within the basement.

1 Introduction

Geophysical integration has been gaining traction in recent years, be it from the joint or cooperative point of views. A number of approaches for the joint modelling have been developed with the goal of exploiting the complementarities between different datasets (see for instance the reviews of Lelièvre and Farquharson, 2016, and Moorkamp et al., 2016, and references therein). As summarized in the review of Ren and Kalscheuer (2019), "joint inversion of multiple geophysical datasets can significantly reduce uncertainty and improve resolution of the resulting models", be it for the modelling of a single property (e.g., resistivity for joint controlled-source electromagnetic and magnetotelluric MT data, or density for joint gravity anomaly and gradiometry data), or of multiple properties (e.g., the joint inversion of seismic and gravity data to model P-velocity and density). In the second case, joint inversion approaches can be grouped into two main categories based on the hypothesis they rely on. Structural approaches allow to jointly invert datasets with differing sensitivities to the properties of the subsurface through the premise that geology is such that spatial changes in inverted properties should be collocated. Structural constraints can then be used as a way to link two or more datasets jointly inverted for by encouraging structural similarity between the inverted models (Haber and Oldenburg, 1997; Gallardo and Meju, 2003). Alternatively, petrophysical approaches utilise prior petrophysical information (e.g., from outcrops, boreholes, or the literature) to enforce certain statistics in the recovered model so that it resembles the petrophysical measurements' (Lelièvre et al., 2012; Sun and Li, 2015; Giraud et al., 2017; Astic and Oldenburg, 2019). Whereas structural and petrophysical approaches are well suited to exploit complementarities between datasets in a quantitative manner, running joint inversion might be, in practice, challenging and requires significantly more computing power than the separate inversions.

In this contribution, we present a new multidisciplinary modelling workflow that, instead of the more common simultaneous joint inversions, relies on sequential, cooperative modelling. It follows the same objectives as the two categories of joint inversion mentioned above in that structural information is passed from one domain to the other and it uses petrophysical information to link domains. The development of the sequential inversion scheme we present was motivated by a similar idea as Lines et al. (1988) who states that "the inversion for a particular data set provides the input or initial model estimate for the inversion of a second data set". A further motivation was to design a workflow capable of integrating the inversion of two or more datasets quantitatively using standalone modelling engines that run independently. The general concept behind the methodology we present is summarised in Figure 1.

In this paper, the workflow is applied to the sequential inversion of magnetotelluric (MT) followed by magnetic data, taking into account the importance of robustly constraining the thickness of the regolith in hard rock imaging and mineral exploration. This is motivated by the relative paucity of works considering cooperative workflows to integrate MT and magnetic data together with the recent surge in interest for the characterisation of the depth-to-basement interface in mineral exploration, despite these two geophysical methods being part of the geoscientists' toolkit for depth-to-basement imaging. Historically, MT has often been integrated with other electromagnetic methods or with seismic data, and with gravity to a lower extent (see review of the topic of Moorkamp, 2017). It is, however, seldom modelled jointly with magnetic data unless a third dataset is considered (e.g., Oliver-Ocaño et al., 2019 ; Zhang et al., 2020; Gallardo et al., 2012; Le Pape et al., 2017). We surmise that this is because (1) the interest for integrating MT with other disciplines arose primarily in oil and gas and geothermal studies and relied on structural similarity constraints for reservoir or (sub)salt imaging, (2) of the difference in terms of spatial coverage between the two methods elsewhere, (3) the differences in terms of sensitivity to exploration targets and (4) the difficulty to robustly correlate electrical conductivity and magnetic susceptibility. Bearing these considerations in mind, we developed a workflow incorporating MT and magnetic inversion with petrophysical information and geological prior knowledge.

In the workflow we develop, we exploit the differences in sensitivity between MT and magnetic data. On the one hand, the MT method, used in a 1D probabilistic workflow as presented here, is well-suited to recover vertical resistivity variations and interfaces, especially in a sedimentary basin environment (Seillé and Visser, 2020). MT data are, however, poorly sensitive to resistors, especially when they are overlaid by conductors (e.g., Chave et al., 2012), which makes it difficult to differentiate between highly resistive features, such as intra-basement resistive intrusions. On the other hand, magnetic data inversion is more sensitive to lateral magnetic susceptibility changes and to the presence of vertical or tilted structures or anomalies. Bearing this in mind, we first derive structural information across the studied area in the form of probability distributions of the interfaces between geological units, extracted from the interpolation of the results the 1D probabilistic inversion of MT data. From there, the probability of occurrence of geological units can be estimated in 2D or 3D. These probabilities are used to divide the area into domains where only specific units can be observed (e.g., basement, sedimentary cover, or both). Such domains are then passed to magnetic data inversion, where they are combined with prior petrophysical information to derive spatially varying bound constraints that are enforced using the alternating direction method of multipliers or 2D or 3D inversion (see Ogarko et al., 2021a, for application to gravity data using geological prior information). Finally, uncertainty analysis of the recovered magnetic susceptibility model is performed and rock unit differentiation allows to control the compatibility of magnetic inversion results with the MT data. The workflow is summarised in Figure 1.

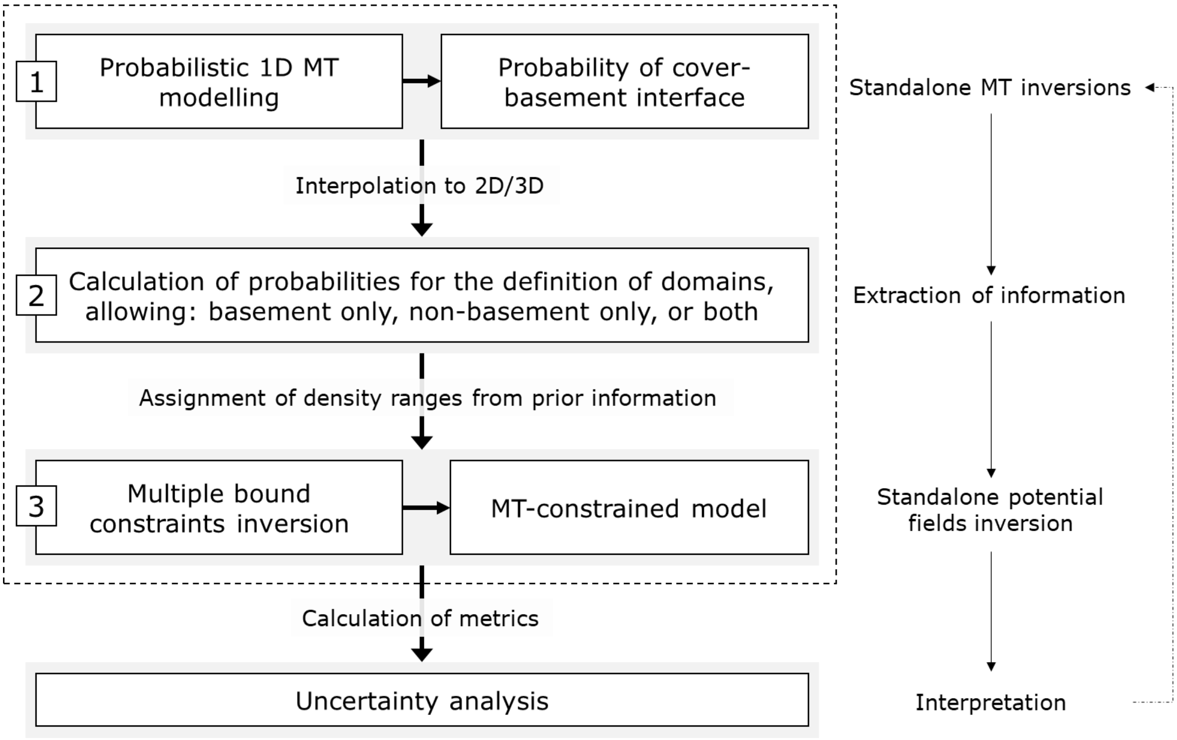

Figure 1. Integrated MT-magnetic integration workflow summary showing the role of the different techniques.

The rem[illegible]d of this paper is organised as follows. We first introduce the methodology and summarise the MT and magnetic standalone modelling procedures we rely on. We then introduce the proof-of-concept in detail using a realistic synthetic case study based on a model of the Mansfield area (Victoria, Australia), which we use to explore the different possibilities for integrating MT-derived information and petrophysics offered by our workflow. Following this, we present a field application using data from Cloncurry (Queensland, Australia) where we tune our approach to the specificity of the area. Finally, this work is placed in the broader context of geoscientific modelling and perspectives for future work are exposed in the discussion section.

2 Methodology

2.1. MT inversion for interface probability

The MT method is a natural source electromagnetic method. Simultaneous measurements of the fluctuations of the magnetic and electric fields are recorded at the Earth's surface under the assumption of a source plane wave. The relationship between the input magnetic field **H** and the induced electrical field **E**, which depends on the distribution of the electrical conductivities in the subsurface, is described by the impedance tensor **Z**, as follows:

$$\mathbf{E} = \mathbf{Z} \cdot \mathbf{H}. \quad (1)$$

Resistivity models derived from MT data are found by forward modelling and inversion of the impedance tensor **Z**, generally using gradient-based deterministic methods (see, e.g., Rodi et al., 2012). Deterministic approaches provide a single solution which minimizes the objective function considered during the inversion, but limited information of the uncertainty around this model can be derived. A global characterization of the uncertainty is possible using a Bayesian inversion framework, but its expensive computing cost limits its application to approximated and/or fast forward modelling solvers (Conway et al., 2018; Manassero et al., 2020; Scalzo et al., 2019). In this study we alleviate this by considering a 1D behaviour of the Earth. While this assumption can stand within layered sedimentary basins, it may fail in more complex geological environments. As we describe below, we account for this source of uncertainty within our Bayesian inversions.

Within the context of Bayesian inversion, the solution of the inverse problem consists in a posterior probability distribution, calculated from an ensemble of models that fits the data within its error. The posterior probability distribution $\mathrm{p}(\boldsymbol{m}^{\boldsymbol{MT}}|\boldsymbol{d}^{\boldsymbol{MT}})$ is obtained using Bayes' theorem, defined as:

$$\mathrm{p}(\boldsymbol{m}^{\boldsymbol{MT}}|\boldsymbol{d}^{\boldsymbol{MT}}) \propto \mathrm{p}(\boldsymbol{d}^{\boldsymbol{MT}}|\boldsymbol{m}^{\boldsymbol{MT}}) \times \mathrm{p}(\boldsymbol{m}^{\boldsymbol{MT}}). \quad (2)$$

The prior distribution $\mathrm{p}(\boldsymbol{m}^{\boldsymbol{MT}})$ contains prior information on the model parameters $\boldsymbol{m}^{\boldsymbol{MT}}$. In this work, we assume a relatively uninformed prior knowledge, using a uniform prior distribution on the electrical resistivity bounds with values set between 10^{-2} and $10^{6}\ \Omega.\mathrm{m}$. Using a uniform prior with such wide boundaries allows the inversion to be mainly data-driven and to remain independent from assumptions about the distribution of electrical resistivity into the Earth. A Gaussian likelihood function $\mathrm{p}(\boldsymbol{d}^{\boldsymbol{MT}} \mid \boldsymbol{m}^{\boldsymbol{MT}})$ defining the data fit is used is used:

$$\mathrm{p}(\boldsymbol{d}^{\boldsymbol{MT}} \mid \boldsymbol{m}^{\boldsymbol{MT}}) \propto \exp\left(-\frac{1}{2}(\boldsymbol{d}^{\boldsymbol{MT}} - g^{MT}(\boldsymbol{m}^{\boldsymbol{MT}}))^{\mathrm{T}}\, \mathbf{C}_{\mathrm{d}}^{-1}\, (\boldsymbol{d}^{\boldsymbol{MT}} - g^{MT}(\boldsymbol{m}^{\boldsymbol{MT}}))\right) \quad (3)$$

The term inside the exponential is the data misfit, which is the distance between observed data $\boldsymbol{d}^{\boldsymbol{MT}}$ and simulated data $g^{MT}(\boldsymbol{m}^{\boldsymbol{MT}})$, scaled by the data covariance matrix $\mathbf{C}_d$, which defines data errors and their correlation across frequencies. We consider two main sources of uncertainty to calculate $\mathbf{C}_d$:

- data processing errors, which we model introducing a matrix $\mathbf{C}_p$;
- errors introduced by the violation of the 1D assumption when using 1D models, which we model introducing $\mathbf{C}_{dim}$.

To calculate $\mathbf{C}_d$, we first define $\mathbf{C}_p$, the covariance matrix accounting for the EM noise and measurement errors, which is estimated during MT data processing. In this study we assume uncorrelated processing noise across frequencies, reducing $\mathbf{C}_p$ to a diagonal matrix. Following this, we define $\mathbf{C}_{dim}$ as the covariance matrix accounting for the discrepancy between 1D models and the multi-dimensional Earth the data is sensitive to. The analysis of the characteristics of the MT phase tensor allows to detect 2D and 3D effects present in the MT data as a function of frequency (see Caldwell et. al., 2004).

Following a dimensionality error model developed by Seillé and Visser (2020) for depth to cover mapping applications, we translate the phase tensor parameters into dimensionality uncertainties to compensate for the limitations of the 1D assumption when performing 1D inversion. This dimensionality uncertainty $\mathbf{C}_{dim}$ is added to the existing data uncertainty $\mathbf{C}_p$, such that the inversion considers both sources of uncertainty in $\mathbf{C}_d$, which we calculate as $\mathbf{C}_d = \mathbf{C}_p + \mathbf{C}_{dim}$. The 1D MT trans-dimensional Markov chain Monte Carlo algorithm used in this study (Seillé and Visser, 2020) solves for the resistivity distribution at depth, and the number of layers in the model and takes as input the determinant of the impedance tensor **Z**. The output of the probabilistic inversion consists in an ensemble of models describing the posterior probability distribution.

In this paper, we are interested in the depth of the basement. For each MT sounding, each model of the model ensemble is analysed and the transitions from a conductive sedimentary layer into a resistive basement is extracted in order to construct a probability distribution of the depth to basement interface. This feature extraction relies on assumptions made on the electrical resistivity of the different lithologies expected, which are formulated on a case by case basis. We first calculate the depth to basement interface probability p_{int} for each MT sounding. These probabilities are derived for each MT sites and can be interpolated on the mesh used for magnetic inversion. The interpolation of such probability distributions can be performed using different approaches and integrate various types of geophysical or geological constraints. In this work, we use a linear interpolation scheme in the synthetic case study, and the Bayesian Estimate Fusion algorithm of Visser and Markov (2019) in the case study. We note that other techniques could be used for a similar purpose, such as the Bayesian Ensemble Fusion (Visser, 2019; Visser et al., 2021), or discrete and polynomial trend interpolations (Grose et al., 2021). Following this, assuming a sedimentary basin lying on top of the basement, we can define for each model cell the probability of being in presence of the basement p_{bsmt} as:

$$p_{bsmt} = P_{int}, \tag{4}$$

with P_{int} the cumulative distribution function of the probability function p_{int}, from the surface downwards. Consequently, for each cell within the model, the probability of being in presence of sedimentary rocks, p_{sed}, is given as $p_{sed} = 1 - p_{bsmt}$.

This allows us to derive three domains characterised by $p_{sed} = 0$ (basement only), $p_{sed} \in]0,1[$ (basement and non-basement units allowed) and $p_{sed} = 1$ (non-basement only) that will define the intervals used for the bounds constraints B applied to magnetic data inversion as summarised below.

2.2. Formulation of the magnetic data inverse problem

In this section, we summarise the method used to enforce disjoint interval bound constraints during magnetic data inversion. We largely follow Ogarko et al. (2021a), which we extend to locally weighted bound constraints. The geophysical inverse problem is formulated in the least-squares sense (see chap. 3 in Tarantola, 2005). The cost function we minimize during inversion is given as:

$$\theta(\boldsymbol{d^{mag}}, \boldsymbol{m^{mag}}) = \|\boldsymbol{d^{mag}} - g^{mag}(\boldsymbol{m^{mag}})\|_2^2 + \alpha_m{}^2 \left\|\boldsymbol{W_m}\left(\boldsymbol{m^{mag}} - m_p^{mag}\right)\right\|_{\boldsymbol{2}}^2 + \alpha_g{}^2 \left\|\boldsymbol{W}_g \nabla \boldsymbol{m^{mag}}\right\|_{\boldsymbol{2}}^2, \tag{5}$$

where $\boldsymbol{d^{mag}}$ is the observed data and $g^{mag}(\boldsymbol{m^{mag}})$ the forward response produced by model $\boldsymbol{m^{mag}}$, a vector of $\mathbb{R}^n$, with n is the total number of model-cells. The second term corresponds to the model damping (or smallness) term, with weight α_m, depth weighting operator $\boldsymbol{W_m}$; m_p^{mag} is the prior model. The operator $\boldsymbol{W_m}$ is defined following Portniaguine and Zhdanov (2002). The third term is the gradient damping (or smoothness) term. The diagonal matrix $\boldsymbol{W}_g$ adjusts the strength of the regularization. It is modulated by α_g (introduced in details in the next section).

We solve eq. (4) while constraining the inversion using multiple bound constraints. The problem can be expressed in its generic form as:

$$\begin{aligned} &\text{minimize } \theta(\boldsymbol{d}, \boldsymbol{m}) \\ &\text{s.t. } m_i \in \mathcal{B}_i, 1 \leq i \leq n \end{aligned} \tag{6}$$

where $\mathcal{B}_i$ is the interval, or set of intervals, binding the i^{th} model-cell. The general definition of B_i is:

$$B_i = \cup_{l=1}^{L_i} [a_{i,l}, b_{i,l}], \text{with } b_{i,l} > a_{i,l}, \forall\, l \in [1, L_i] \text{ and } i \in \mathcal{I} \tag{7}$$

where $a_{i,l}$ and $b_{i,l}$ define, the bounds of the inverted property l is the index of the rock unit; L_i is the number of bounds in the i^{th} interval; $\mathcal{I}$ contains the indices of the model-cells where the bound constraints are applied. A summary of the algorithm solving this problem using the alternating direction method of multipliers technique (ADMM) is given in Appendix A.

2.3. Integration with MT modelling

The set of intervals $\mathcal{B}$ from eq. (6) and (7) can be defined homogenously across the entire model or accordingly with prior information. In the latter case, it allows to define spatially-varying bound constraints and to activate them only is selected parts of the study area. In the case presented by Ogarko et al. (2021a), probabilistic geological modelling was used to determine such bounds constraints for gravity inversion. The approach we propose here follows the same philosophy. Instead, we use probabilistic MT modelling, which can be used to estimate the observation probabilities of rock units. From such probabilities, we can then calculate the bounds B_i for the i^{th} model-cell using:

$$B_i = \bigcup_{\substack{l=1 \\ P_{i,l} > P_{t,l}}}^{L_i} \left[a_{i,l}, b_{i,l}\right], \tag{8}$$

where $P_{i,l}$ is the observation probability for the l^{th} rock unit; $P_{t,l}$ is a threshold value above which the probability is considered sufficiently high to be considered. In what follows we use $P_{t,l} = 0$.

2.4. Uncertainty metrics

2.4.1. Model misfit

In the synthetic study we present, we evaluate the capability of inversions to recover the causative model using the root-mean-square (RMS) misfit between the true and inverted models (RMS model misfit). We calculate this indicator as:

$$ERR_m = \sqrt{\frac{\mathbf{1}}{n}\sum_{i}^{n}\left(m_i^{true} - m_i^{inv}\right)^{\mathbf{2}}}, \tag{9}$$

where $\boldsymbol{m}^{\boldsymbol{true}}$ and $\boldsymbol{m}^{\boldsymbol{inv}}$ are, respectively, the true and inverted models.

2.4.2. Membership analysis

In the context geophysical inverse modelling, membership analyses provide a quantitative estimation of interpretation uncertainty to interpretation of recovered petrophysical properties. Using the intervals defined in eq. (7) and eq. (8), we apply a triangular function to the inverted magnetic susceptibilities to determine the membership values to the different rock types. For the i^{th} model cell, the membership value to the j^{th} rock type ω_j^i is calculated using ramp functions as:

$$\omega_j^i = \begin{cases} 1 \; if \; m^i \in B_k \vee m^i \geq b_{i,\mathrm{L}} \; if \; k = L \vee m^i \leq a_{i,1} \; if \; if \; k = 1 \\ \dfrac{m^i - b_{i,\mathrm{j}-1}}{a_{i,\mathrm{j}} - b_{i,j-1}} \; if \; b_{i,\mathrm{j}-1} \leq m^i \leq a_{i,\mathrm{j}} \\ \dfrac{a_{i,\mathrm{j}+1} - m^i}{a_{i,\mathrm{j}+1} - b_{i,j}} \; if \; b_{i,\mathrm{j}} \leq m^i \leq a_{i,\mathrm{j}+1} \\ 0 \; otherwise \end{cases} \tag{10}$$

2.4.3. Total model entropy

Using the membership values ω, we calculate the total model entropy of the model, H, which is the arithmetic mean of the information entropy (Shannon, 1948) of all model-cells:

$$H = -\sum_{k=1}^{M}\sum_{i=1}^{L} \omega_k^i \log\left(\omega_k^i\right), \tag{11}$$

which is as a measure of geological uncertainty in probabilistic models and of the fuzziness of the interfaces (Wellmann and Regenauer-Lieb, 2012).

2.4.4. Jaccard distance

In addition to calculating H, the membership values ω can be used to interpret the inversion results in terms of rock units. The index k of the rock unit the model-cell with a given inverted magnetic susceptibility value can be interpreted as is given as, for the i^{th} model-cells:

$$k = \arg\max_{j=1..L} \omega_j^i. \tag{12}$$

Calculating the index of the corresponding rock unit in each model-cell, we obtain a rock unit model $\boldsymbol{m}_U^{\boldsymbol{inv}}$.

Using $\boldsymbol{m}_U^{\boldsymbol{inv}}$ and $\boldsymbol{m}_U^{\boldsymbol{true}}$ (the latter being the true rock unit model), we calculate the Jaccard distance (Jaccard, 1901), which is a metric quantifying the similarity between discrete models. In the context of geological modelling, it is reflective of the dissimilarity between geological models (Schweizer et al., 2017). Here, we use it to compare the inverted model and the true model as follows:

$$J = 1 - \frac{\left|\boldsymbol{m}_U^{\boldsymbol{true}} \cap \boldsymbol{m}_U^{\boldsymbol{inv}}\right|}{\left|\boldsymbol{m}_U^{\boldsymbol{true}} \cup \boldsymbol{m}_U^{\boldsymbol{inv}}\right|} = \frac{\left|\boldsymbol{m}_U^{\boldsymbol{true}} \cup \boldsymbol{m}_U^{\boldsymbol{inv}}\right| - \left|\boldsymbol{m}_U^{\boldsymbol{true}} \cap \boldsymbol{m}_U^{\boldsymbol{inv}}\right|}{\left|\boldsymbol{m}_U^{\boldsymbol{true}} \cup \boldsymbol{m}_U^{\boldsymbol{inv}}\right|}, \tag{13}$$

where $\cap$ and $\cup$ are the intersection and union of sets, respectively; $|\cdot|$ is the cardinality operator, measuring the number of elements satisfying the condition. A useful and simple interpretation of J is that it represents the fraction of cells assigned with the incorrect rock unit.

3 Synthetic case study

The synthetic case study that we use to test our workflow was built using a structural geological framework initially introduced in Pakyuz-Charrier et al. (2018. It presents realistic geological features that reproduce field geological measurements from the Mansfield area (Victoria, Australia). The choice of resistivity and magnetic susceptibility values to populate the structural model was made to test the limits of this sequential, cooperative workflow and to show its potential to alleviate some of the limitations inherent to potential field and MT inversions. To this end, we selected a part of the synthetic model ~~which~~ features violate the hypothesis of a 2D model to challenge the workflow we propose.

3.1. Survey setup

The structural geological model was derived from foliations and contact points using the Geomodeller® software (Calcagno et al., 2008; Guillen et al., 2008; Lajaunie et al., 1997). It is constituted of a sedimentary syncline abutting a faulted contact with a folded basement. The model's complexity was increased with the addition of a fault and an ultramafic intrusion. Details about the original 3D geological model are provided in Pakyuz-Charrier et al. (2018b). Here, we increased the maximum depth of the model to 3150 m and added padding in both horizontal directions. Figure 2a shows the non-padded 2D section extracted from the reference 3D geological model.

We assigned magnetic susceptibility in the model considering non-magnetic sedimentary rocks in the basin units (lithologies 3, 5 and 6 in Table 1) and literature values (see Lampinen et al., 2016) to dolerite (lithology 4), diorite (lithology 2) and ultramafic rocks (lithology 1). We assign electrical resistivities assuming relatively conductive sedimentary rocks and resistive basement and intrusive formations. Resistivities in sedimentary rocks might vary orders of magnitude, and mainly depend on porosity, which is linked to the degree of compaction and the type of lithology, and the salinity of pore fluid (Evans et al., 2012). The three sedimentary layers were assigned different resistivities values, of 30 Ωm, 10 Ωm and 50 Ωm for basin fill 3, 2 and 1 respectively (see Table 1), basin 1 being the oldest and deeper formation. Metamorphic and intrusive rocks as found in the crust generally present high resistivities (Evans et al., 2012). In what follows we focus on the modelling of data located along the line shown in Figure 2, simulating the modelling magnetic data in 2D, while considering 3D MT data. The modelled rock units and their petrophysical properties are given in Table 1. The geological, magnetic susceptibility and resistivity true models are shown in Figure 2.

Table 1 Stratigraphic column showing geological topological relationships and average physical properties. Lithologies are indexed from 1 through 6 by order of genesis.

Lithology index	Geological relation	Geological unit	Magnetic susceptibility (SI)	Electrical resistivity (Ωm)
6	Sedimentary	Basin fill 3	0	30
5	Sedimentary	Basin fill 2	0	10
4	Intrusive	Dolerite	0.025	5000
3	Sedimentary	Basin fill 1	0.0001	50
2	Intrusive	Diorite	0.025	5000
1	Basement	Ultramafic rocks	0.05	2000

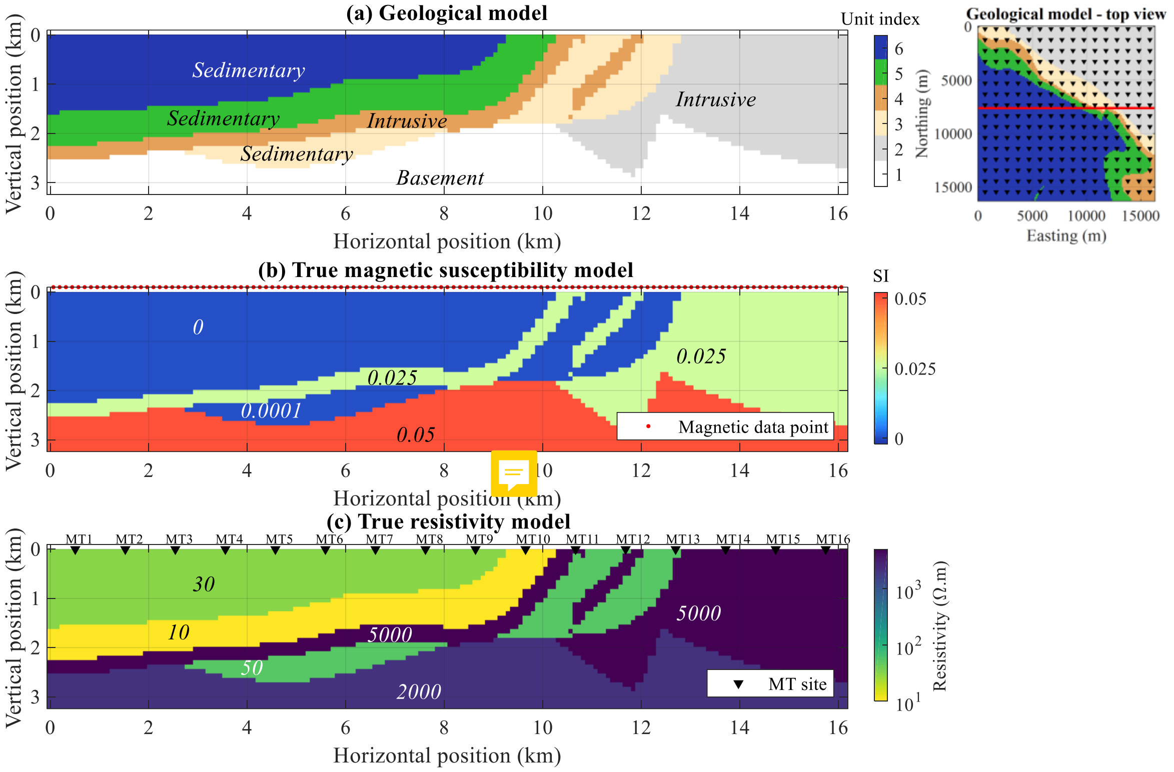

Figure 2. (a) True geological model (b) true magnetic susceptibility model and (c) true resistivity model with the simulated MT acquisition setup geometry in the top-left corner where triangles represent MT sites. The red dots in (b) represents the 2D magnetic data line; MT sites are marked in (c). The inset in the top-right corner shows a top view of the model with the magnetic data line in red and MT sites as triangles.

3.2. Simulation of geophysical data

3.2.1. Magnetic data

The core 2D model is discretised into $N_x \times N_y \times N_z = 1 \times 128 \times 36$ cells of dimensions equal to $127 \times 127 \times 90$ m^3. We generate one magnetic datum (reduced to pole magnetic intensity) per cell along the horizontal axis, leading to 128 data point. To limit dispersion effects, we add 10 padding cells perpendicular to the profile and extend it by 36 cells at each extremity along its length, leading to $N_x \times N_y \times N_z = 11 \times 192 \times 36$ cells of dimensions $381 \times 127 \times 90$ m^3. The reference magnetic susceptibility model used for forward data computation is shown in Figure 2.

Airborne magnetic data were simulated for a fixed wing aircraft flying at an altitude of 100 m above topography. The forward solver we use follows Bhattacharyya (1964) to model the total magnetic field anomaly. In this example, we model a magnetic field strength equal to 57,950 nT. It corresponds to the International Geomagnetic Reference Field for the Rawlinna station, Western Australia.

We add normally distributed noise with an amplitude equal to 2.5% of the average amplitude of the data. We simulate noise contamination by adding noise sampled randomly from by a normal distribution characterised by a standard deviation of 3.8 nT and a mean value of 0 nT. For the simulation of geological "noise", we then apply a Gaussian filter to such random noise to obtain spatially correlated values. The uncontaminated and noisy data are shown in Figure 3. For the inversion, the objective data misfit is set accordingly with the estimated noise.

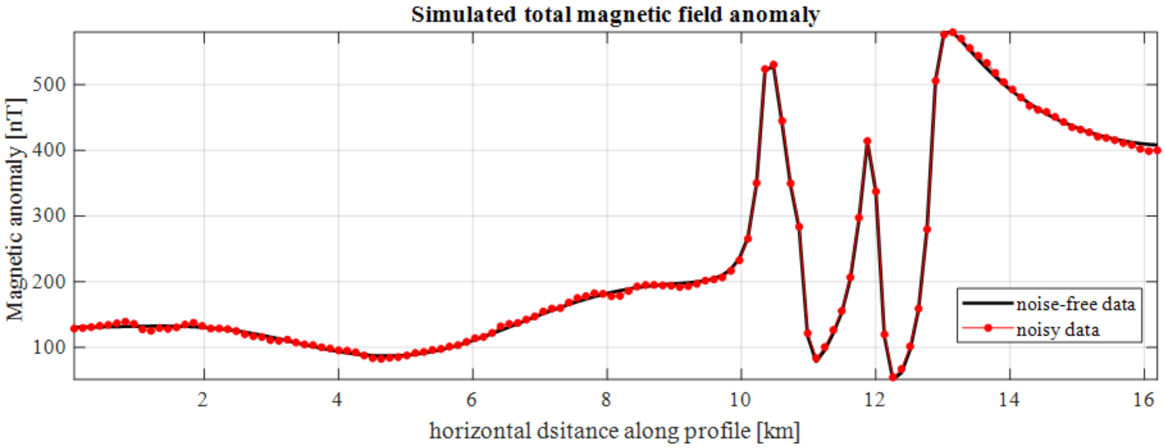

Figure 3. Simulated total magnetic field anomaly.

3.2.2. MT data

The synthetic MT data is computed using the complete 3D resistivity model derived from the 3D geological model, to simulate the influence of 3D effects. The core of the electrical conductivity model used the same discretization as the magnetic susceptibility model. Relationships between geological units and electrical resistivities follow Table 1. A padding zone was added in both horizontal directions and vertically, in order to satisfy the boundary conditions required by the forward solver. The final mesh has 160 x 160 x 62 cells in the x, y and z directions, respectively. The ModEM 3D forward modelling code (Egbert and Kelbert, 2012; Kelbert et al., 2014) was used to simulate the MT responses of this model. The MT responses were computed at 256 stations evenly spaced 1.016 km on a 16×16 grid (see inset in Figure 2). The frequency range spans from 10 KHz to 0.01 Hz, with 6 frequencies per decades, for a total of 37 frequencies; 5% magnitude Gaussian white noise was added to the synthetic data before running the 1D inversions.

In the following subsections, we present the results of the modelling of synthetic data along a 2D section (see Figure 2c) from the 3D resistivity volume, following the workflow proposed in Sect. 2. Along this section, 16 MT sites are used. We start with the modelling of MT data to derive constraints and prior information for the inversion of magnetic data.

3.3. 1D Probabilistic inversion of MT data and derivation of cover-basement interface probabilities

We perform the 1D MT inversions of each MT sounding independently, using a 1D trans-dimensional Markov chain Monte Carlo sampler (Seillé and Visser, 2020). The presence of 2D and 3D effects was compensated for using larger uncertainties, calculated using the workflow introduced in Seillé and Visser (2020) and summarized in Sect. 2.1.

All the 1D trans-dimensional Bayesian inversions ran using 60 Markov chains with 10^6 iterations each. For each chain, a burn-in period of 750,000 samples (75% of the total) was applied to ensure convergence, after which we recorded 100 models equidistantly spaced. The model ensembles are then constituted by 6000 models for each MT site. An example of the posterior distribution for three MT sites is shown in Figure 4. The distribution of interfaces within the posterior ensemble of 1D models is described by a change-point histogram. Figure 4a and Figure 4b show the model posterior distribution for MT sites MT1, MT8 and MT16.

From the posterior ensembles of models and interfaces, a depth to basement probability distribution is calculated independently for each MT site. For this synthetic case, we simply assume that the transition from the sedimentary cover to the basement occurs when a layer L1 of resistivity $\rho_1 < \rho_X$ is followed by a layer L2 of resistivity $\rho_2 > \rho_X$, with $\rho_X = 200\ \Omega\text{m}$. As mentioned in Sect. 2.1, this process is applied to each model of the ensemble and allows the extractions of geological features of interest from the posterior model ensemble. If less than 0.1 % of the all transitions observed in the ensemble presents the feature defined earlier using ρ_X, we then assume that the transition is not observed. This situation occurs for MT sites MT14, MT15 and MT16 (see Figure 4c for site MT16). Figure 4 shows the interface probability and the depth to basement interface probability p_{int} for three selected sites along the profile.

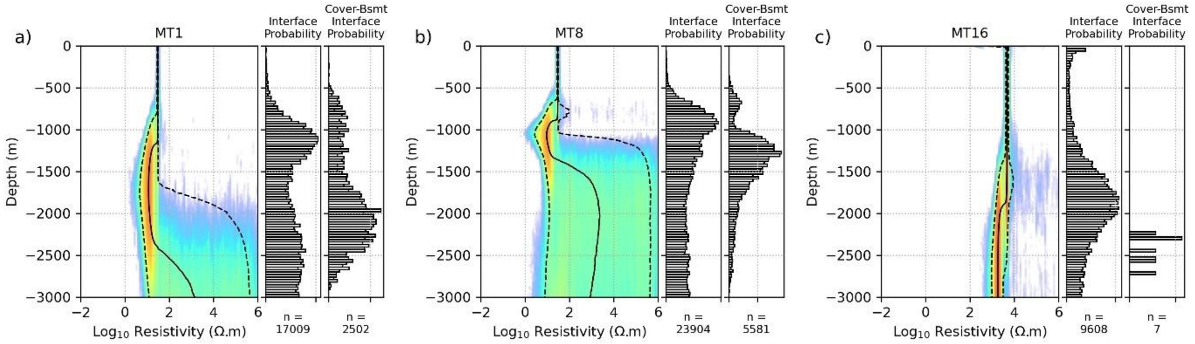

Figure 4. Example of posterior distribution of resistivity for three MT sites MT1 in (a), MT8 in (b) and MT16 in (c), located along the profile as shown in Figure 2, with the interface probability distribution and cover-basement interface probability distribution. The number of transitions observed in the posterior interface distribution is indicated. Site MT1 (a) is located in the western part of the profile in the basin, site MT8 (b) is located in the middle part of the profile, in the basin, and site MT16 (c) is located in the eastern part where the intrusive rock unit outcrops (see Figure 2c). High probabilities in the model posterior distribution is represented by warms colours, and low probabilities with cold colours. The dashed lines represent the 5th and the 95th percentiles of the model posterior distribution and the black line represents the median of the model posterior distribution. The values of 'n' correspond to the number of values used in the corresponding plots.

3.4. Deriving constraints for magnetic inversion

3.4.1. Bound constraints

Starting from P_{int} values calculated for each MT site, we interpolate the probabilities from MT onto the mesh used for magnetic data inversion. In this synthetic example, we use a linear interpolation scheme. The interpolated probabilities from MT are shown in Figure 5.

The interpolated probabilities are used to define domains for the application of bound constraints during magnetic data inversion. In this example, we complement information from MT inversions with the assumption that dolerite outcrops and is mapped accurately (unit 4, intrusive, see Table 1 and Figure 2). Using this, we adjust the domains for the corresponding few model-cells at surface level, only at two locations where we assume these outcrop to be known. The domains for the bound constraints we obtain are shown in Figure 5c, domains 1 and 2 indicate parts of the model where MT inversion suggests a single rock unit. This means that in the corresponding model cells, a single interval will be used in the definition of the bound constraints, while two intervals will be used otherwise.

3.4.2. Prior model

The prior model for magnetic inversion is obtained using the MT derived rock unit probabilities (Figure 5a-c) and the magnetic susceptibility of the rock units given in Table 1. We calculate it as follows, for the ith model-cell:

$$\left(\boldsymbol{m}_{\boldsymbol{p}}^{\boldsymbol{mag}}\right)_{\boldsymbol{i}} = \sum_{j=1}^{L} \psi_i^j a_{i,j}. \qquad (14)$$

We chose to use $a_{i,j}$, the lower bound for each rock unit (or group of rock units), as it constitutes the most conservative assumption about magnetic susceptibility from the range of plausible magnetic susceptibilities. The resulting prior model is shown in Figure 5d.

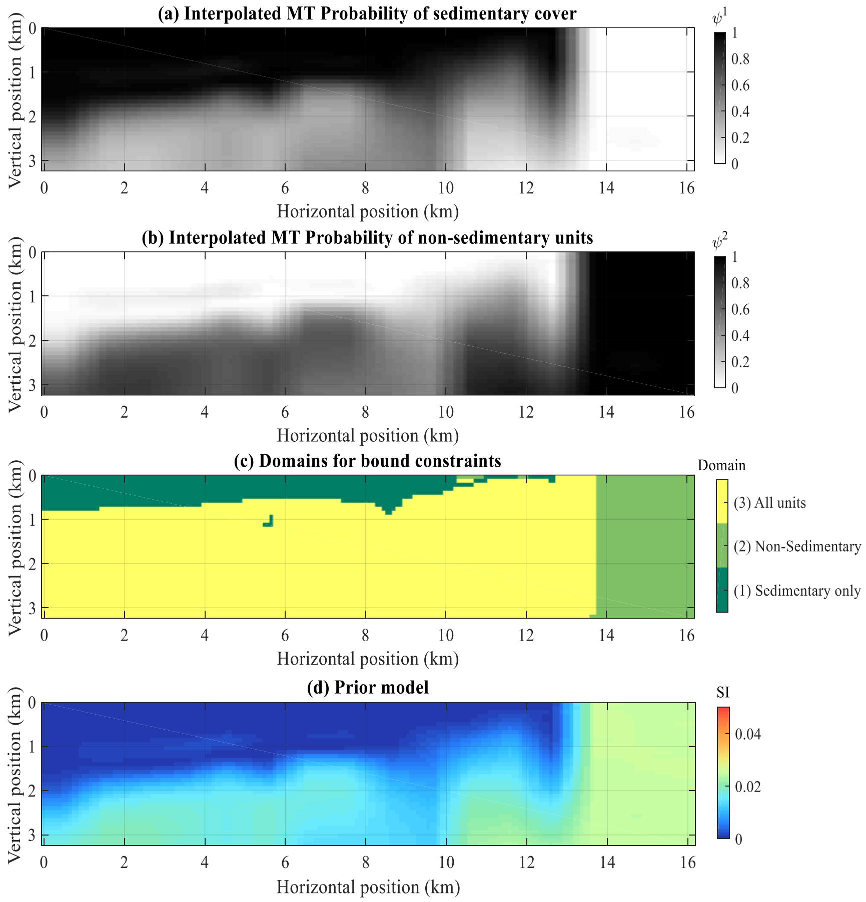

Figure 5. Interpolated probability of sedimentary cover (a) and non-sedimentary units (b), corresponding domains (c), and (d) prior model from MT derived rock unit probabilities and magnetic susceptibility rock units observed in the area. The location of the simulated MT sites is reminded in (a).

3.5. Inversion of magnetic data and uncertainty analysis

In this section, we study the influence of MT-derived prior information onto magnetic inversion and estimate the related reduction of interpretation uncertainty. The different scenarios tested here are summarized in

Table **2**, while the corresponding in version results are shown in Figure 6.

Table 2. Scenarios tested for the utilisation of MT-derived information in magnetic data inversion. 'High confidence' refers to the case where constraints are applied only where MT-derived rock units probabilities are equal to 1.

Case scenario	Prior model	ADMM bound constraints	Smoothness constraints
(a) Unconstrained inversion	Homogenous	None	Global
(b) High confidence bounds constraints only (domains 1 and 2 only)	Homogenous	Only where MT shows high confidence	Global
(c) Global bound constraints	Homogenous	Homogenous, all model-cells	Global
(d) Global bound constraints with prior model	MT-derived	Homogenous, all model-cells	Global
(e) Local bound constraints with prior model	MT-derived	Locally defined, all cells	Global
(f) Local bound constraints and smoothness, with prior model	MT-derived	Locally defined, all cells	Locally weighted

(a) Unconstrained inversion

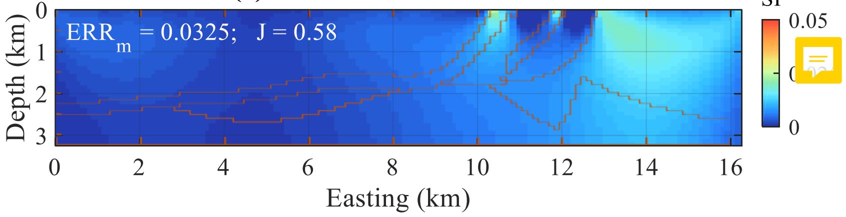

(b) High confidence bounds constraints only

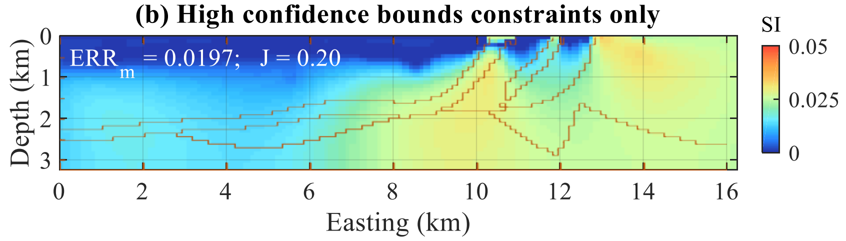

(c) Global bound constraints

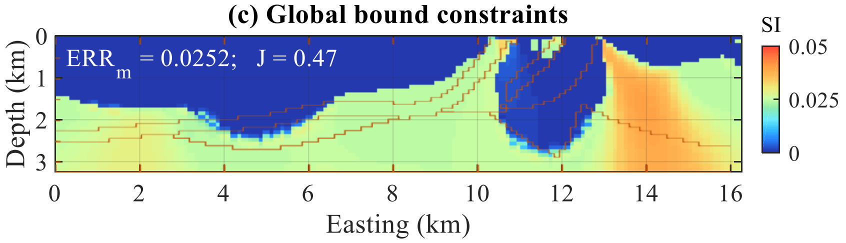

(d) Global bound constraints with prior model

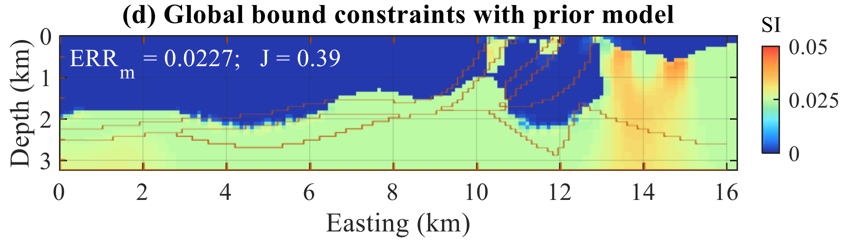

(e) Local bound constraints with prior model

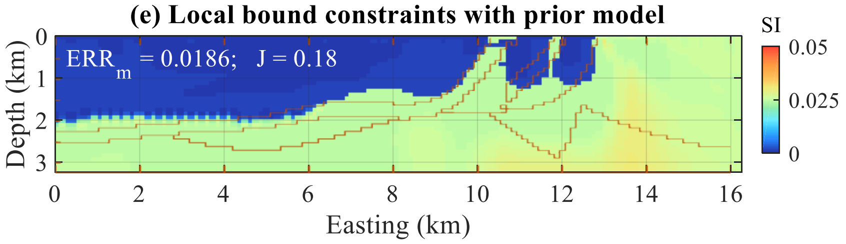

(f) Local bound constraints and smoothness with prior model

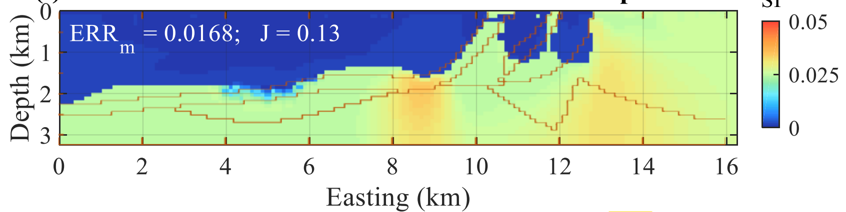

Figure 6. Inversion results for the different scenarios tested. Cases (a) through (e) correspond to inversions using prior information and constraints summarised in

Table 2. The brown lines materialise the interfaces between geological units in the true model. ERRm refers to the RMS model misfit.

We complement the calculation of ERR_m and J (see values in Figure 6) with the membership analysis following eq. (10) as a measure of interpretation uncertainty. The resulting membership values are shown in Figure 7, where we added the values of the model's information entropy H.

(a) Unconstrained inversion

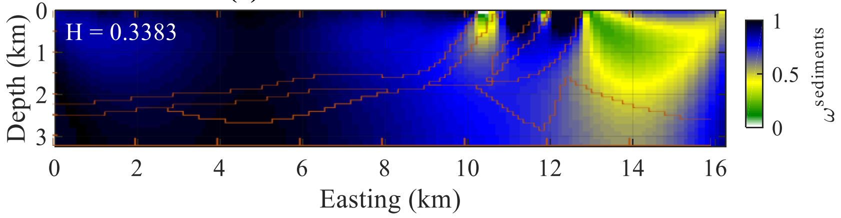

(b) High confidence bounds constraints only

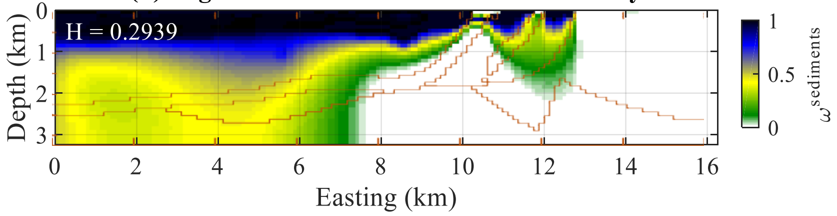

(c) Global bound constraints

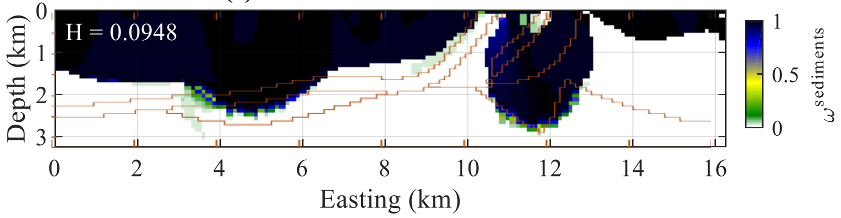

(d) Global bound constraints with prior model

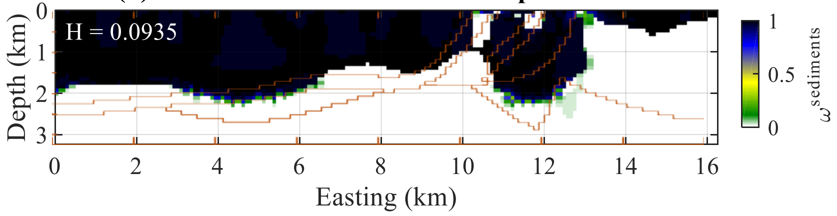

(e) Local bound constraints with prior model

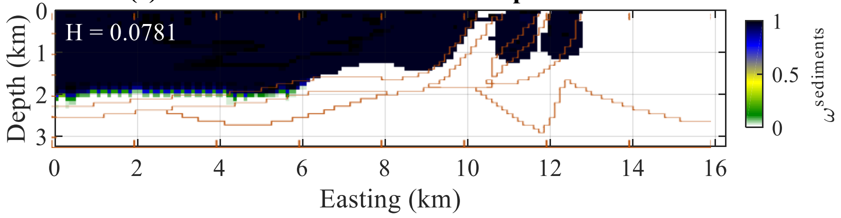

(f) Local bound constraints and smoothness with prior model

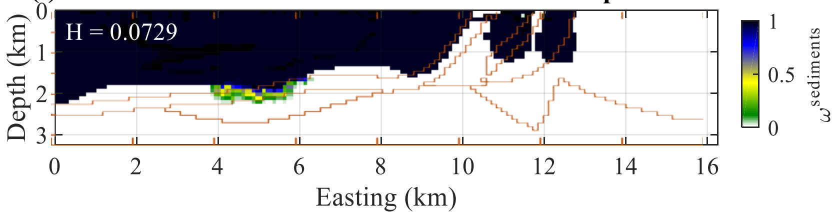

Figure 7. Membership values for the non-magnetic lithologies. Cases (a) through (e) correspond to inversions using prior information and constraints summarised in

Table **2. The brown lines materialise the interfaces between geological units in the true model. H refers to the information entropy of the model (eq. 11).** 365

A visual comparison of the membership values in Figure 7e and Figure 7f with the MT-derived domains (Figure 5c) indicates good consistency with MT domains (1) and (2) (single rock units inferred). It also shows that the proposed workflow has the capability to improve the recovery of the sedimentary cover thickness significantly when compared to cases that do not use MT-derived ADMM constraints across the entire model (Figure 7a, b and c).

To complete our analysis, we propose a simple metric combining two statistical indicators by weighting the RMS model misfit resulting from geophysical inversion (ERR_m) with the corresponding entropy values (H), which reflect geological interpretation uncertainty. Figure 8 shows the apparent relationship between the amount of prior information and constraints used in inversion and the proposed indica[illegible] We observe a continuous reduction of $H \times ERR_m$ from case (a) to (f), indicating a progression towards models that are closer to the true model and less ambiguous to interpret. Overall, together with values of the Jaccard distance J (Figure 6), our testing reveals that, using MT-derived ADMM constraints provides inversions results that are the closest to the true model. However, it also suggests that from case (c) to (f), the impact of additional constraints decreases comparatively to cases (a) to (c). It also indicates that using the prior model has a limited effect on inversion, as cases (a) and (c) show similar values in Figure 8 and the corresponding models in Figure 6 and Figure 7 present similar features.

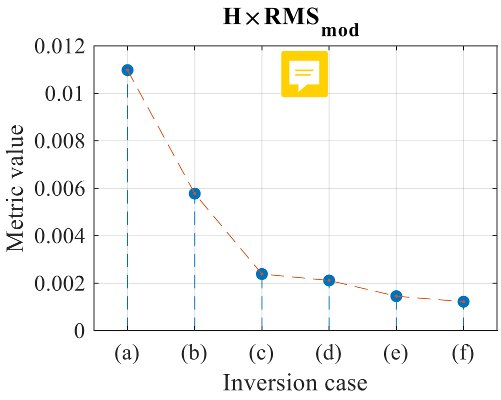

Figure 8. Uncertainty metric $H \times ERR_m$ for inversion cases (a) through (f).

4 Field case study

We propose an application example illustrating potential utilisations of the proposed sequential inversion workflow. Using observations made in the synthetic case, our aim here is to integrate MT with magnetic data inversion using the case relying on MT-derived ADMM bound constraints with homogenous starting model and smoothing constraints. We note that, to the best of our knowledge, this is the first time that the ADMM algorithm is used to constrain magnetic data inversion.

We used existing results of the depth to basement derived using MT within a probabilistic workflow (Seillé et al., 2021) in the Cloncurry area in Queensland (see Figure 9). These results are used to constrain the magnetic inversion.

4.1. Geoscientific context and area of interest

The depth to basement interface probability used for the magnetic inversion was derived by Seillé et al. (2021). Using a similar workflow as presented in sections 2.1 and 3.3, they derived a cover-basement interface distribution for each MT site using the model posterior distribution obtained using 1D probabilistic inversions. Then, a probabilistic depth to basement interface across the survey area was derived combining these MT depth to basement estimates with drill-hole depth-to-basement estimates, constrained by a structural model in the form of interpreted faults across the area. The combination of estimates coming from different sources of information to derive a posterior distribution on the depth to basement was performed using the Bayesian Estimate Fusion algorithm of Visser and Markov (2019). This probabilistic workflow allowed to obtain a probabilistic map of the depth-to-basement interface. The structural model used during the Estimate Fusion assumed vertical faults, which is a valid assumption given the near vertical behaviour of the main faults in the area (Austin and Blenkinsop, 2008; Case et al., 2018).

The geological map of the area is shown in Figure 9.

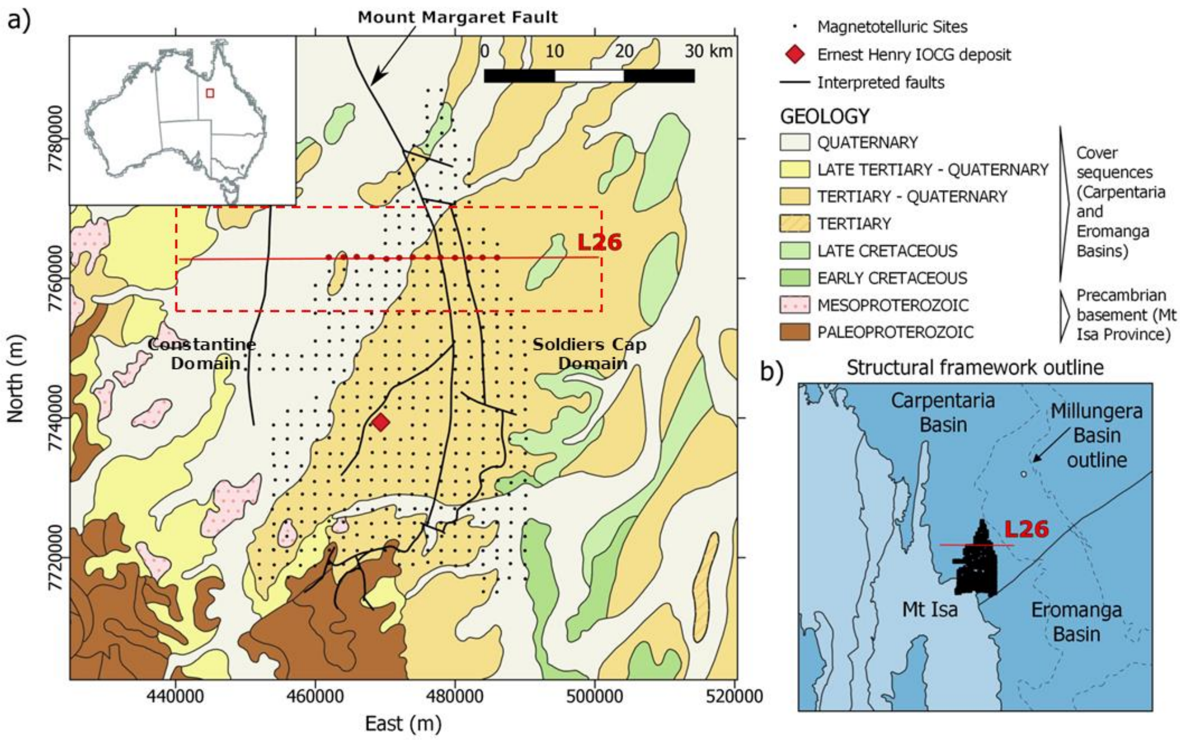

Figure 9. a) Geological map of the area. The small dots are the MT sites of the Cloncurry MT survey. The red line is the profile used in this study, and the red dots are the MT sites associated to this profile. b) Structural framework. Modified from Seillé et al. (2021). The Constantine Domain to the west and the Soldiers Cap Domain to the east are separated by the Mouth Margaret Fault; the red dashed line delineates the area we focus on.

In this study, we focus on a 2D profile (L26, see location on map in Figure 9a), and invert the corresponding magnetic data extracted from the anomaly map shown in Figure 10a and Figure 10b. The choice of an East-West oriented profile was motivated by the North-South orientation of the main structures in the area and by the geological features the known geology and the geophysical measurements suggest. The profile is nearly perpendicular to these structures, making it suitable for use within a 2D inversion scheme. It crosses the North-South oriented Mount Margaret Fault, which is thought to belong to the northern part of the regional Cloncurry Fault structure, a major crustal boundary that runs North-South over the Mount Isa Province (Austin and Blenkinsop, 2008; Blenkinsop, 2008). This boundary separates two major Paleoproterozoic sedimentary sequences (Austin and Blenkinsop, 2008). The geological modelling performed by Dhnaram and Greenwood (2013) also indicates that the Mount Margaret Fault separates two distincts domains, the Constantine Domain to the West and the Soldier Caps Domain to the East. In our study area, the Constantine domain is covered by non-magnetic cover constituted by Mesozoic and Cenozoic sediments, lying on what is believed to be consitituted by the Mount Fort Constantive volcanics, in some places intruded by the Williams Supersuite pluton. On the eastern side, the Soldier Caps Domain is also covered by Mesozoic and Cenozoic sediments, and the basement is interpreted to be a succesion of volcanic and metamorphic rocks (Dhnaram and Greenwood, 2013).

The depth to basement probabilistic surface derived by Seillé et al. (2021) along the W-E profile (see Figure 10c) presents a relatively shallow basement in the western part of the profile (~ 100 meters thick, with some lateral variations). In the eastern part of the profile, the model indicates that a two-steps fault system controls the thickening of the basin to the east. It reaches ~ 350 meters thickness in the eastern part. The depth to basement model along the profile shown in Figure 10c is relatively well constrained by MT and drill hole data. However, the interpolation method we used imposed spatial continuity between estimates that, using MT soundings with relatively large separation (2 km) and sparse drill holes, did not allow for the definition of small-scale depth to basement lateral variations. Significant lateral variations were allowed during the interpolation using the fault traces indicated by the structural data, defining areas where discontinuities are expected (in the location of the faults), to encourage a relaxation of the spatial continuity and to allow for sharp jumps. The magnetic data shown in Figure 10a suggest that other faults and other lateral discontinuities could exist.

In this work, we assume a non-magnetic sedimentary cover, and a magnetic basement. In addition, we assume little to no remanent magnetization and little to no self-demagnetisation. Important remanence and self-demagnetization can be observed in the vicinity of magnetite-rich IOCG deposits (e.g., Anderson and Logan, 1992; Austin et al., 2013), but we consider that there is no indication of such features along L26. Further to this, we make this assumption for the sake of simplicity as the main object of this paper is the introduction of a new sequential inversion workflow and to show that it is applicable to field data.

Under these premises, the features the magnetic data presents can be exploited to improve the image of the cover-basement interface when integrated with prior information about the thickness of cover. In this context, the role of magnetic data inversion constrained by MT is therefore multiple:

- to constrain the depth and extent of the magnetic anomalies and refine their geometry;
- to analyse the compatibility between the constraints derived from MT and the magnetic data and resolve some small-scale structures not defined by the MT constrains;
- to reduce the interpretation uncertainty of the cover-basement interface;
- to propose new scenarios in relation to the composition of the basement (in terms of its magnetic susceptibility) and structure (through its lateral variations).

The depth of the cover-basement interface probability shown in Figure 10c is used to derive the domains required by the spatially varying bound constraints using in magnetic inversion.

4.2. Constrained Magnetic data inversion

4.2.1. Magnetic data preparation and extraction of prior information

We use the gridded reduced-to-pole (RTP) magnetic data from the Geological Survey of Queensland shown in Figure 10 (https://geoscience.data.qld.gov.au/dataset/ds000018/resource/91106497-d463-4b83-8b01-1c5539ab40b1, last accessed on 27/07/2021). Prior to the 2D inversion of the data along the line L26, we manipulate and reformat the data. To account for variations in the measurements in the vicinity of the line, we extract data from a 800 meters wide band around the profile (L26) (Figure 10a), as shown in more details Figure 10a. To obtain data corresponding to a 2D rectilinear profile, we then calculate the weighted average of this subset of the dataset by assigning weights inversely proportional to the square of the distance of the measurement to L26, as illustrated in Figure 10b.

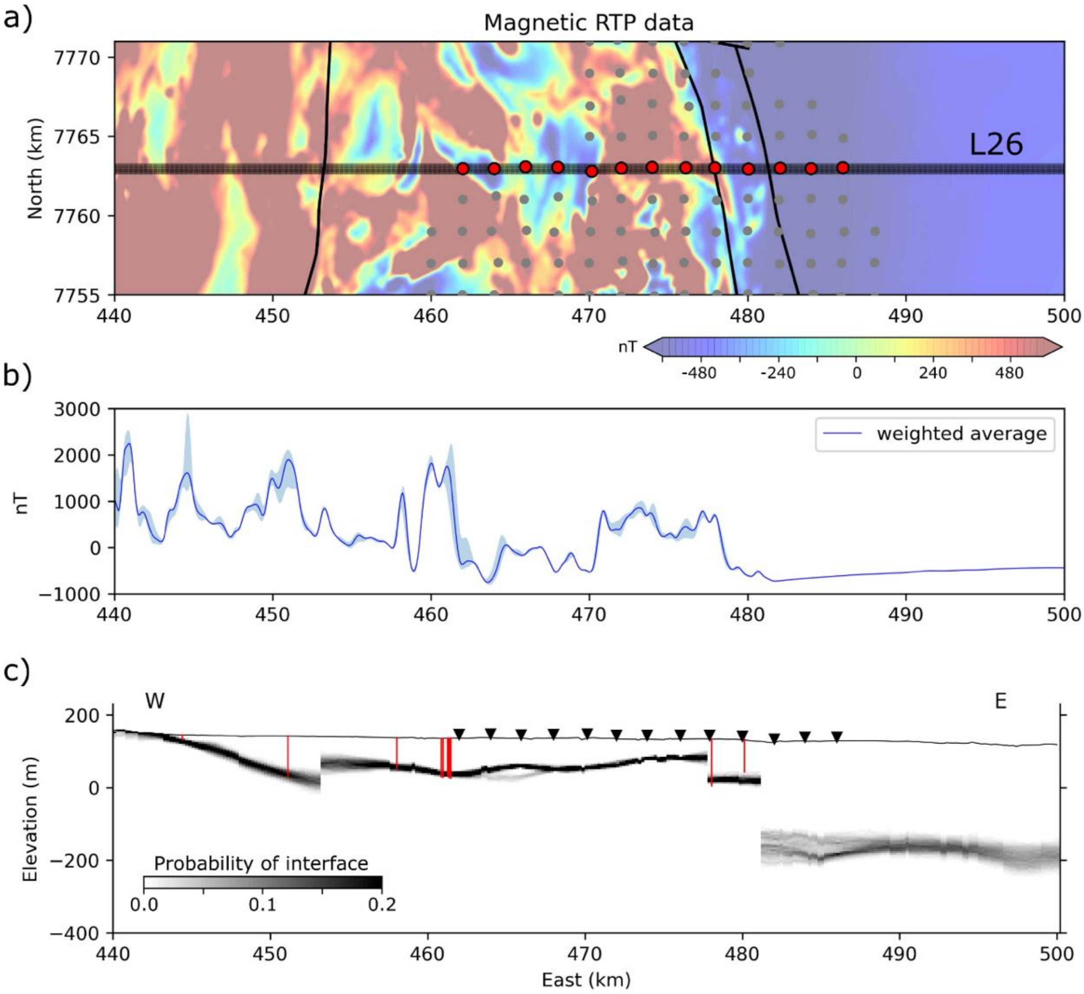

Figure 10. Data preparation. (a) map view of the data in the region of interest. The grayed-out area corresponds to the zone considered for the averaging of the magnetic data. Red points are MT soundings considered in this study. Grey circles are others MT soundings not used in this study. (b) shows data for magnetic inversion (solid line) and the envelope of the data from the 800 meters band around L26 (light blue shade). The shades of blue represent the weight assigned to the data points in the calculation of the average: the lighter the shade, the lower the weight. c) Depth of the cover basement interface probability (Seillé et al., 2021). Red lines are the drill holes, and their bottom represent the intersection with the basement. The drill holes plotted are projected a distance up to 800 meters away from the profile.

We convert the interface probability shown in Figure 10c into basement and sedimentary rock probabilities using the method described in Section 2.1 and 3.4.1. We assume that the sedimentary basin domain overlies the basement domain, and derive the corresponding domains for the ADMM bound constraints using the domaining procedure described above. The resulting domains are shown in Figure 11.

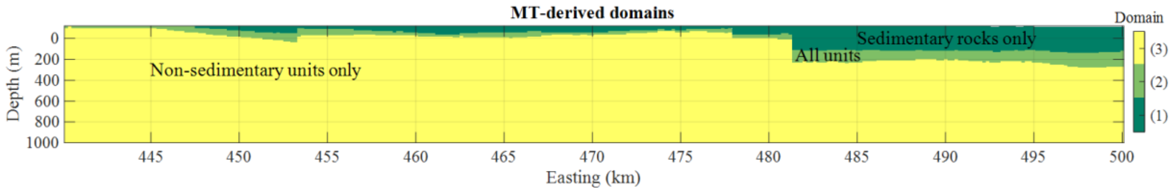

Figure 11. MT-derived domains for cases with (1) sedimentary units only, (2) sedimentary and non-sedimentary units and (3) non-sedimentary units only.

In what follows, we assume that sedimentary rocks have a low magnetic susceptibility comprised within the range [-0.006, 0.006] SI, while the basement units, mainly composed of volcanic sequences, are modelled to have higher magnetic susceptibilities within the interval [0.015 0.09] SI.

4.2.2. Inversion setup and results

To reduce computing time, we truncate the sensitivity matrix of the magnetic data inverse problem under the assumption that model-cells beyond a given distance exert a negligible influence on the forward calculated data. The sensitivity domain is reduced to a 25 km-radius cylinder of infinite height and depth around each data point in a moving sensitivity domain approach (see examples in Čuma et al., 2012; Čuma and Zhdanov, 2014) that assumes negligible contribution of the models-cells beyond a certain distance from the measurement's location. Using a similar approach, the results of Wilson et al. (2011), indicate that using a 25 km radius may result in approximately 98% accuracy in the calculation of the response, which we assume to suffice for the purpose of our application example. In our case, it allows a reduction of 67% of the size of the sensitivity matrix. We performed inversion using 12 threads on an Intel(R) Xeon(R) CPU E5-2630.

To examine the impact of different type of constraints, we first perform inversions using minimum prior information and successively increase the amount of prior information from unconstrained inversion to using MT-derived intervals for multiple bound constraints. The inversions we run consist of the following cases:

(1) constrained by homogenous smoothness constraints;
(2) constrained by homogenous smoothness constraints with lower and upper bound constraints;
(3) constrained by homogenous smoothness constraints with global, multiple bound constraints;
(4) constrained by homogenous smoothness constraints with local, multiple bound constraints derived from MT.

The results for inversion cases (1) through (4) are shown in Figure 12.

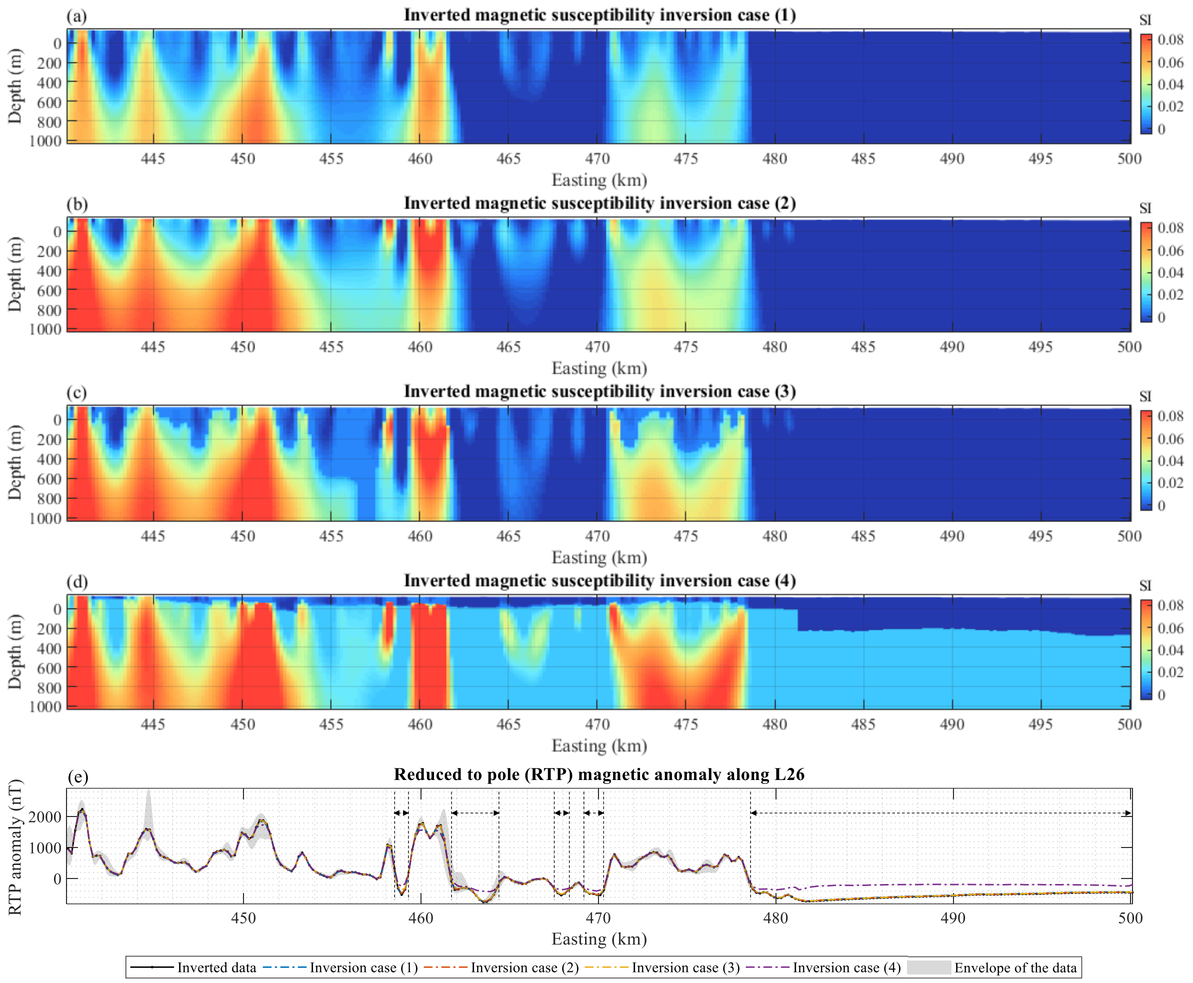

Figure 12. Inversion results. (a) through (d) corresponds to inversion types (1) through (4), respectively. (e) shows the data fit for the 4 inversions shown. The grey shading shows the amplitude of the data shown in Figure 10 for calculating the weighted average of the inverted anomaly. The dashed lines mark the horizontal extension of areas where hypotheses made for magnetic inversion may be incompatible with the data.

The inversions reached a satisfactory data fit, exception made for the constrained inversion 4 (see the data fit in Figure 12e). In that case a significant underfit of the magnetic data is observed within certain areas, which point to an incompatibility between the magnetic data and the constraints applied. Four areas in the central part of the model are slightly underfit, on length scales < 300 meters. On the eastern part of the profile, from 479 km East to the most eastern part of the profile, an important underfit is observed. At this stage, this data misfit can indicate that the constraints used are not appropriate. This could be due to an inexact positioning at depth of the structural constrains, or to a change in the petrophysical behaviour of the basement in certain areas, which would link differently the electrical properties of the depth to basement constrains to their magnetic properties. We propose a 5th inversion case where we adjust the bounds manually to examine hypotheses relaxing the constraints derived by the combination of MT inversions and the magnetic susceptibility of rocks in the area.

From Figure 12, we identify five main areas where hypotheses made for the utilisation of MT-derived domains need to be adjusted. In each case, the domain allowing sedimentary units may be deeper than expected or the basement may be less susceptible. We test the plausibility of such alternative scenarios and adapt the MT-derived domains by adjusting the domains. We increased the depth of the non-sedimentary (i.e., basement) units in the eastern part of the model and between the areas marked by dashed lines in Figure 12, where the basement-sedimentary interface may be deeper than anticipated or the basement characterized by less susceptible rocks. The domains we use after adjustment are shown in Figure 13a, and inversion results in Figure 13b and c, respectively. Figure 13d proposes an automated interpretation using membership values ω using eq. (18); t[illegible]uestion marks identify areas where the initial hypotheses have been revisited and which may require further investigations. The arrows point to parts of the model where the basement may be at the shallowest l[illegible] authorised by MT.

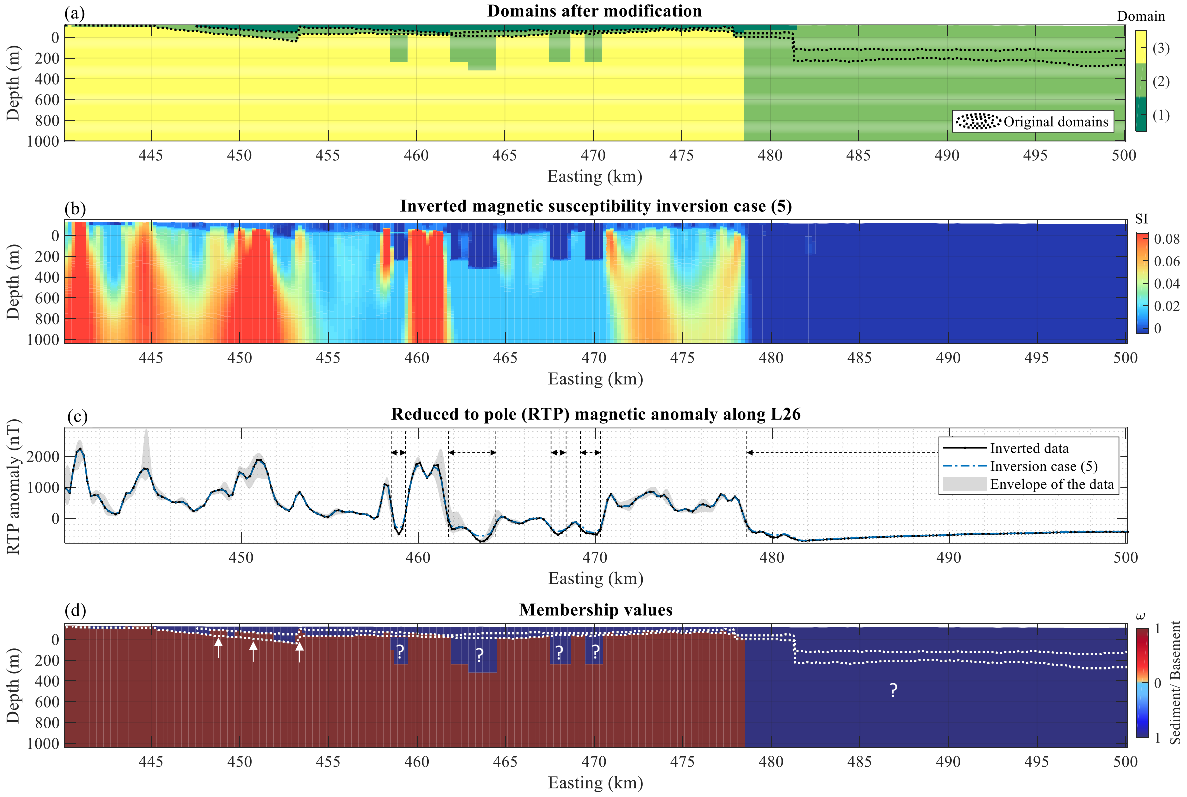

Figure 13. (a) MT-derived domains adjusted following the adjustments suggested by magnetic data inversion, for domains with (1) sedimentary units only, (2) sedimentary and non-sedimentary units and (3) non-sedimentary units only. (b) is the inverted model for inversion case (5) and (c) is the inverted and field magnetic RTP data, with the horizontal extent of the locations where MT bounds were adjusted; (d) shows the membership values to the sedimentary and basement units obtained using eq. (10), overlaid with the original contours of MT-derived domains. In (c), the grey shading shows the envelope of the data shown in Figure 10 for calculating the weighted average of the inverted anomaly.

Beyond the possibility to revisit hypotheses made at earlier stages of the workflow, we get insights into the structure and magnetic susceptibility of the basement. While electrical conductivity and magnetic susceptibility may be sensitive to change in rock type, there are scenarios where they exhibit differing sensitivity to texture and grain properties, respectively. For instance, metamorphism and alteration might affect electrical conductivity and magnetic susceptibility differently (Clark, 2014; Dentith et al., 2020). Under these circumstances, our results can provide insights into plausible geological processes given sufficient prior geological information about the deformation history.

4.3. Interpretation

From a multi-physics modelling point of view, the results shown in the previous Sect. shows a general agreement between the MT-derived constraints and the magnetic data. However, the results also point to incompatibilities in a few parts of the model. We identified two major areas where incompatibility occurs:

1) ~~a~~ smaller inconsistent areas in the western part of the survey;

2) a large inconsistent area east of the Mount Margaret Fault.

We interpret these incongruencies as being mainly due to the different sensitivities of the two geophysical methods to different geological features and to the petrophysical variability of the basement in the area.

The greater depth extent of some of the lower magnetic susceptibility zones required by the magnetic data in the western part of the survey suggests that the depth to magnetic source is greater than suggested by the constraints. Adjustments to the constraints allowed a better data fit. A low magnetic response between kms 460 and 470 East (Figure 10) is assumed to be the response to low magnetic susceptibilities and is interpreted to be granitic intrusions of the William-Naraku Supersuite (Dhnaram and Greenwood, 2013). The presence of such intrusions offers a plausible explanation for the discrepancies between the magnetic and MT modelling. On the one hand, the MT data modelling might not able to distinguish between an electrically resistive basement and an electrically resistive intrusion, while the magnetic data modelling could not distinguish between a non-magnetic cover and a non-magnetic intrusion. On the other hand, magnetic data inversion can differentiate the low susceptibility intrusion from the higher susceptibility volcanic rocks, and the MT data is sensitive to the basal cover interface above both the volcanic rock and the intrusion. The constrained inversion permits detection of the lateral extent of the intrusion while estimating cover thickness. While detailed modelling of higher resolution data would be required to refine the geometry of these intrusive bodies, our modelling suggests that the intrusion could be modelled as several smaller intrusions.

East of the Mount Margaret Fault, the incompatibility between the original MT-derived constraints and the magnetic data points to regional scale structures. Drill hole observations indicate basement not exceeded 350 meters depth. If we assume a high-susceptibility basement, which is common to the whole area (Dhnaram and Greenwood, 2013), the magnetic model requires a very thick non-magnetic cover layer to reconcile the data which is incompatible with our geological knowledge of the area. In that case, we need to reconsider our definition of the basement. The north-trending Mount Margaret Fault (see Figure 9) separates two geological domains exhibiting different basement characteristics. East of the Fault is the Soldiers Cap domain and is predominantly non-magnetic volcanic rocks. By relaxing the geological model constraints in that part of the model both sedimentary and non-sedimentary units are allowed (Figure 11a) and we can satisfactorily fit the data. The necessity of considering non-magnetic volcanic rocks in the Soldier Caps domain agrees with the magnetic modelling performed by Dhnaram and Greenwood (2013).

5 Discussion

We have presented a workflow for sequential joint modelling of geophysical data, and applied it to synthetic and field measurements. In this study we used constraints in the form of interface probabilities derived from a probabilistic workflow driven by MT data, but it is general in nature and is not limited to a particular geological or geophysical modelling method to generate the inputs. This has allowed us to report the utilisation of the ADMM algorithm to constrain magnetic data inversion for the first time

This workflow presents several advantages. It is computationally inexpensive by use of standalone inversions. The inversion of the MT dataset used to derive the constraints was performed only once. Then, a series of constrained magnetic inversions was run to test different geophysical and petrophysical hypotheses. It shows the example of a fast and flexible approach to test different structural and petrophysical assumptions while modelling data sensitive to different physical parameters. It allows to focus the modelling efforts on survey-specific features (anomalies, geological structures) when appropriate petrophysical information is available. However, as with generalizable methods, strengths become limitations under certain circumstances. For instance, in the case of MT and magnetic data inversions as proposed in this work, the electrical resistivity and magnetic susceptibility for the rock types of interest is dependent on a range of factors and processes (such as porosity, permeability, rock alteration, etc.) such that their correlation may be case-dependant (see Dentith et al., 2020; Dentith and Mudge, 2014). While we may surmise that it remains reasonable to assume the existence of such correlation in hard rock scenarios, it may not always hold in basin environments. For example, one can easily think of a basin exploration case where electrical resistivity increases rapidly with increasing hydrocarbon concentration in reservoirs, while changes in magnetic susceptibility might make the use of magnetic data inversion redundant. In such case, other property pairings can be considered, such as electrical resistivity and seismic attributes (see examples of Le et al., 2016; Tveit et al., 2020, who use seismic inversion to extract prior information for CSEM inversion). Further to this, the utilisation of magnetic data inversion for the deeper part of the crust is limited to depths shallower than the Curie point's (typically from approximately 10 to a few 10s of kilometres under continents). For deeper imaging of the crust, the workflow we propose may be suited to the utilisation of gravity data with MT.

An assumption worth examination is whether the study area is adequately represented by two geological domains. In the cases we investigated, these domains were defined by the probability of observing only two rock classes (basement and non-basement). While this assumption reduces the risk of misinterpretation as no hypotheses are made to distinguish between the different sedimentary units or rocks of different nature in the basement, it also then limits the interpretations that can be made from the results presented. We expect that provided that the rock units present 'desirable' features, i.e., distinctive magnetic susceptibility and resistivities (or other properties depending on the geophysical techniques considered) several rock types can be considered in the modelling. Such discriminative aspects of the petrophysics needs to be ascertained while defining the number of distinctive domains that may be present in the study area. This necessarily requires robust petrophysical data to be available given the strong constraint that these domains impart on inversion. However, in the absence of petrophysical data or the number and character of geological domains, the magnitude of misfit can inform whether a proposed number of domains is plausible, driving data acquisition or refinement of the conceptual geological model. Methods that exploit this approach remain to be investigated further in future case studies.

The application case was performed in 2D to illustrate the workflow. Extending the presented work to large scale problems in 3D is straightforward as the inversion methods employed in this study were designed for 3D modelling. The 1D MT modelling and interpolation schemes present excellent scalability. The Tomofast-x engine (Giraud et al., 2021b; Ogarko et al., 2021b) is implemented using 3D grids. It presents good scalability and it offers the possibility to reduce the size of the computation domain to save memory when calculating the sensitivity matrix in the same fashion as Čuma et al. (2012), and Čuma and Zhdanov (2014), for large-scale potential field data modelling. On this basis, the workflow presented here might be applicable to large datasets using, for instance, MT data from the EarthScope USArray MT program (http://www.usarray.org/researchers/obs/magnetotelluric/, last accessed on 10/09/2021) or the AusLAMP program (https://www.ga.gov.au/eftf/minerals/nawa/auslamp, last accessed on 10/09/2021) and combined with publicly available potential field data. Studies of this kind would span continents for crustal investigations to discover tectonic discontinuities and terrane interfaces. Current investigations on Tomofast-x comprise the application of wavelet compression operators to accelerate the inversion in the same way as Li and Oldenburg (2003) and Martin et al. (2013) and the development of joint inversions using the ADMM constraints for multiple bound constraints.

Another straightforward extension of the workflow is the use of gravity data simultaneously with, or instead of, magnetic data since it is already implemented in Tomofast-x (Giraud et al., 2021b). Giraud et al. (2020) presented a synthetic MT-constrained gravity inversion, using a similar workflow as the one presented here. This would be of particular interest in the Cloncurry region (Queensland, Australia), where for instance, Moorkamp (2021) recently investigated the joint inversion of gravity and MT data, and where our workflow could be applied using the MT modelling results of Seillé et al. (2021).

From a geophysical point of view, magnetic inversion is affected by the non-uniqueness of the solution to the inverse potential field problem despite prior information and constraints being used. The workflow could be improved by using a series of models representative of the geological archetypes that can be derived from the ensembles of 1D MT models. Geological archetypes are distinctly different structural configurations (or topologies) that plausibly exist for a given location with available data (Pakyuz-Charrier et al., 2019, Wellmann and Caumon, 2018). Identification of the archetypes could be achieved from the ensemble of geological model realisations in the same spirit as Pakyuz-Charrier et al. (2019), who use a Monte Carlo approach to generate a range of topologies which are then examined for distinct clusters which represent the archetypes.

From a methodological point of view, it could be argued that simultaneous joint geophysical inversion combining structural and petrophysical constraints might outperform the workflow we proposed here. However, this would make the modelling process more demanding combined with limitations based on cases where determining the causitive relationships between petrophysics supporting joint approaches poses a challenge. The workflow we propose here presents a few advantages over a joint inversion scheme, in the sense that it does not require both datasets to be inverted simultaneously under a defined set of petrophysical and/or structural constraints. The time required to run a joint inversion being limited by the running time of the more computationally expensive technique, it can limit the range of tests to be performed. In this study, we could run rapidly many 2D constrained magnetic inversions, even if the 1D probabilistic inversions of the MT data (and posterior fusion) required significant longer running time compared to the 2D constrained magnetic inversion. This point would particularly be relevant in the case of large 3D datasets. This approach may represent a step in the modelling workflow which that is useful to explore, understand and refine structural and petrophysical relationships between different physical parameters before undertaking more demanding joint inversions.

In the field application case presented here, the probabilistic depth to basement map to derive ~~constraint~~ assumed lateral continuity of the depth to basement estimates at a large scale, not accounting for small-scale lateral variations. Thus, uncertainty for depth to basement may be underestimated at some locations, in particular in between MT sites ~~as~~ shallow depths. In such cases, the existence of incompatibilities between MT-derived constraints and the magnetic data might require reconsidering the spatial continuity assumptions taken during the calculation of the probabilistic depth to basement surface. Extensions of this work may be devised to alleviate some of the limitations of the workflow. For instance, magnetic susceptibility from the inversion of magnetic data could be mapped back to a resistivity model in order to calculate forward MT data for validation (dashed line in Figure 1), or to constrain the next cycle of MT inversions in the case the workflow is extended to cooperative joint inversion. It would also be straightforward to use to a level-set inversion that can consider an arbitrary number of geological units (e.g., Giraud et al., 2021) using MT modelling as a source of prior information and constraints. We have used hard bounds using the ADMM algorithm, which can easily be complemented or replaced by the use of multi-modal petrophysical distributions as available in Tomofast-x (e.g., mixture models as in Giraud et al., 2017, 2019) as an alternative.

6 Conclusion

We have introduced, tested on synthetic, and applied to field data a cooperative inversion scheme for the integration of MT and magnetic inversions. We have shown that despite its simplicity, the workflow we propose efficiently leverages the complementarities between the two methods and has the capability to improve our understanding of the cover-basement interface and of the basement itself. We have tested our workflow on a synthetic study that illustrates the flexibility of the method and the different possibilities our workflow offers as well as their limitations. In the field application case (Cloncurry area, Queensland), we have shown how the quantitative integration of MT and magnetic data may bring insightful results on geological structural and petrophysical aspects, opening up new avenues for interpretations of the geology of the area and prompting future works.

7 Authors' contribution

JG and HS designed the study with inputs from the rest of the authors. JG and HS and generated the magnetic and MT synthetic data, respectively. JG performed the magnetic data inversions. JG redacted the manuscript with inputs from HS who is the main contributor to MT-related aspects, and comments from the rest of the authors. HS performed the synthetic MT data modelling, with support from GV. HS and GV derived the MT depth to basement results used in the case study. ML and MJ provided geological support and knowledge. ML participated in both the geological and geophysical interpretation of the results and edited the relevant sections of the manuscript. ML provided detailed comments during its redaction. GV participated in the design of the methodology and the interpretation of results.

VO and JG worked together on the development of functionalities of Tomofast-x that are introduced and applied in the presented work. All authors provided feedback on the different versions of the manuscript and during the progress of the study.

8 Competing interests

The authors declare that they have no conflict of interest.

9 Acknowledgements

JG, ML and MJ are supported, in part, by Loop – 25 Enabling Stochastic 3D Geological Modelling (LP170100985) and the Mineral Exploration Cooperative Research Centre whose activities are funded by the Australian Government's Cooperative Research Centre Program. This is MinEx CRC Document 2021/36. ML is supported by ARC DECRA DE190100431. HS and GV are supported by the CSIRO Deep Earth Imaging Future Science Platform. We acknowledge the developers of the ModEM code to make it available.

10 Data and code availability

The modified version of the structural model of Pakyuz-Charrier (2018) used here is given in Seillé and Giraud (2021). It also contains the synthetic MT and magnetic data used. The field data can be obtained from the Geological Survey of Queensland.

The version of the Tomofast-x inversion code used here was made publicly available by Ogarko et al. (2021b); the latest version is available at: https://github.com/TOMOFAST/

11 References

Anderson, C. G. and Logan, K. J.: The history and current status of geophysical exploration at the Osborne Cu & Au deposit, Mt. Isa, Explor. Geophys., 23, 1–7, doi:10.1071/EG992001, 1992.

Astic, T. and Oldenburg, D. W.: A framework for petrophysically and geologically guided geophysical inversion using a dynamic Gaussian mixture model prior, Geophys. J. Int., 219, 1989–2012, doi:10.1093/gji/ggz389, 2019.

Austin, J. and Blenkinsop, T.: The Cloncurry Lineament: Geophysical and geological evidence for a deep crustal structure in the Eastern Succession of the Mount Isa Inlier, Precambrian Res., 163, 50–68, doi:10.1016/j.precamres.2007.08.012, 2008.

Austin, J. R., Schmidt, P. W. and Foss, C. A.: Magnetic modeling of iron oxide copper-gold mineralization constrained by 3D multiscale integration of petrophysical and geochemical data: Cloncurry District, Australia, Interpretation, 1, T63–T84, doi:10.1190/INT-2013-0005.1, 2013.

Bhattacharyya, B. K.: Magnetic anomalies due to prism-shaped bodies with arbitrary polarization, Geophysics, 29, 517–531, 1964.

Blenkinsop, T.: Mount Isa inlier, Precambrian Res., 163, 1–6, doi:10.1016/j.precamres.2007.08.009, 2008.

Boyd, S.: Distributed Optimization and Statistical Learning via the Alternating Direction Method of Multipliers, Found. Trends® Mach. Learn., 3, 1–122, doi:10.1561/2200000016, 2010.

Calcagno, P., Chilès, J. P., Courrioux, G. and Guillen, A.: Geological modelling from field data and geological knowledge. Part I. Modelling method coupling 3D potential-field interpolation and geological rules, Phys. Earth Planet. Inter., 171, 147–157, doi:10.1016/j.pepi.2008.06.013, 2008.

Case, G., Blenkinsop, T., Chang, Z., Huizenga, J. M., Lilly, R. and McLellan, J.: Delineating the structural controls on the genesis of iron oxide–Cu–Au deposits through implicit modelling: a case study from the E1 Group, Cloncurry District, Australia, Geol. Soc. London, Spec. Publ., 453, 349–384, doi:10.1144/SP453.4, 2018.

Chave, A. D., Jones, A. G., Mackie, R. and Rodi, W.: The Magnetotelluric Method, Cambridge University Press, Cambridge., 2012.

Clark, D. A.: Magnetic effects of hydrothermal alteration in porphyry copper and iron-oxide copper–gold systems: A review, Tectonophysics, 624–625, 46–65, doi:10.1016/j.tecto.2013.12.011, 2014.

Conway, D., Simpson, J., Didana, Y., Rugari, J. and Heinson, G.: Probabilistic Magnetotelluric Inversion with Adaptive Regularisation Using the No-U-Turns Sampler, Pure Appl. Geophys., 175, 2881–2894, doi:10.1007/s00024-018-1870-5, 2018.

Čuma, M. and Zhdanov, M. S.: Massively parallel regularized 3D inversion of potential fields on CPUs and GPUs, Comput. Geosci., 62, 80–87, doi:10.1016/j.cageo.2013.10.004, 2014.

Čuma, M., Wilson, G. A. and Zhdanov, M. S.: Large-scale 3D inversion of potential field data, Geophys. Prospect., 60, 1186–1199, doi:10.1111/j.1365-2478.2011.01052.x, 2012.

Dentith, M. and Mudge, S. T.: Geophysics for the mineral exploration geologist., 2014.

Dentith, M., Enkin, R. J., Morris, W., Adams, C. and Bourne, B.: Petrophysics and mineral exploration: a workflow for data analysis and a new interpretation framework, Geophys. Prospect., 68, 178–199, doi:10.1111/1365-2478.12882, 2020.

Dhnaram, C. and Greenwood, M.: 3D MINERAL POTENTIAL OF THE QUAMBY AREA. [online] Available from: https://geoscience.data.qld.gov.au/report/cr089698, 2013.

Egbert, G. D. and Kelbert, A.: Computational recipes for electromagnetic inverse problems, Geophys. J. Int., 189, 251–267, doi:10.1111/j.1365-246X.2011.05347.x, 2012.

Evans, R. L., Chave, A. D., Jones, A. G., Mackie, R. and Rodi, W.: Conductivity of Earth materials, in The Magnetotelluric Method, pp. 50–95, Cambridge University Press, Cambridge., 2012.

Gallardo, L. a. and Meju, M. a.: Characterization of heterogeneous near-surface materials by joint 2D inversion of dc resistivity and seismic data, Geophys. Res. Lett., 30, doi:10.1029/2003GL017370, 2003.

Gallardo, L. A., Fontes, S. L., Meju, M. A., Buonora, M. P. and de Lugao, P. P.: Robust geophysical integration through structure-coupled joint inversion and multispectral fusion of seismic reflection, magnetotelluric, magnetic, and gravity images: Example from Santos Basin, offshore Brazil, Geophysics, 77, B237–B251, doi:10.1190/geo2011-0394.1, 2012.

Giraud, J., Pakyuz-Charrier, E., Jessell, M., Lindsay, M., Martin, R. and Ogarko, V.: Uncertainty reduction through geologically conditioned petrophysical constraints in joint inversion, GEOPHYSICS, 82, ID19–ID34, doi:10.1190/geo2016-0615.1, 2017.

Giraud, J., Ogarko, V., Lindsay, M., Pakyuz-Charrier, E., Jessell, M. and Martin, R.: Sensitivity of constrained joint inversions to geological and petrophysical input data uncertainties with posterior geological analysis, Geophys. J. Int., 218, 666–688, doi:10.1093/gji/ggz152, 2019.

Giraud, J., Seillé, H., Visser, G., Lindsay, M., and Jessell, M. (2020). Utilisation of stochastic MT inversion results to constrain potential field inversion. EGU General Assembly 2020, Online. https://doi.org/10.5194/egusphere-egu2020-15067

Giraud, J., Lindsay, M. and Jessell, M.: Generalization of level-set inversion to an arbitrary number of geological units in a regularized least-squares framework, GEOPHYSICS, 1–76, doi:10.1190/geo2020-0263.1, 2021a.

Giraud, J., Ogarko, V., Martin, R., Jessell, M. and Lindsay, M.: Structural, petrophysical and geological constraints in potential field inversion using the Tomofast-x v1.0 open-source code, Geosci. Model Dev. Discuss. [preprint], in review, doi:https://doi.org/10.5194/gmd-2021-14, 2021b.

Grose, L., Ailleres, L., Laurent, G. and Jessell, M.: LoopStructural 1.0: time-aware geological modelling, Geosci. Model Dev., 14, 3915–3937, doi:10.5194/gmd-14-3915-2021, 2021.

Guillen, A., Calcagno, P., Courrioux, G., Joly, A. and Ledru, P.: Geological modelling from field data and geological knowledge. Part II. Modelling validation using gravity and magnetic data inversion, Phys. Earth Planet. Inter., 171, 158–169, doi:10.1016/j.pepi.2008.06.014, 2008.

Haber, E. and Oldenburg, D.: Joint inversion: a structural approach, Inverse Probl., 13, 63–77, doi:10.1088/0266-5611/13/1/006, 1997.

Jaccard, P.: Étude comparative de la distribution florale dans une portion des Alpes et du Jura, Bull. la Société Vaudoise des Sci. Nat., 37, 547–579, doi:http://dx.doi.org/10.5169/seals-266450, 1901.

Kelbert, A., Meqbel, N., Egbert, G. D. and Tandon, K.: ModEM: A modular system for inversion of electromagnetic geophysical data, Comput. Geosci., 66, 40–53, doi:10.1016/j.cageo.2014.01.010, 2014.

Lajaunie, C., Courrioux, G. and Manuel, L.: Foliation fields and 3D cartography in geology: Principles of a method based on potential interpolation, Math. Geol., 29, 571–584, doi:10.1007/BF02775087, 1997.

Lampinen, H., Occhipinti, S., Lindsay, M. and Laukamp, C.: Magnetic susceptibility of Edmund Basin, Capricorn Orogen, WA, ASEG Ext. Abstr., 2016, 1–8, doi:10.1071/aseg2016ab254, 2016.

Le, C. V. A., Harris, B. D., Pethick, A. M., Takam Takougang, E. M. and Howe, B.: Semiautomatic and Automatic Cooperative Inversion of Seismic and Magnetotelluric Data, Surv. Geophys., 37, 845–896, doi:10.1007/s10712-

016-9377-z, 2016.

Lelièvre, P., Farquharson, C. and Hurich, C.: Joint inversion of seismic traveltimes and gravity data on unstructured grids with application to mineral exploration, Geophysics, 77, K1–K15, doi:10.1190/geo2011-0154.1, 2012.

Lelièvre, P. G. and Farquharson, C. G.: Integrated Imaging for Mineral Exploration, in Integrated Imaging of the Earth: Theory and Applications, pp. 137–166., 2016.

Li, Y. and Oldenburg, D. ~W.: Fast inversion of large-scale magnetic data using wavelet transforms, Geophys. J. Int., 152, 251–265, doi:10.1046/j.1365-246X.2003.01766.x, 2003.

Lines, L. R., Schultz, A. K. and Treitel, S.: Cooperative inversion of geophysical data, GEOPHYSICS, 53, 8–20, doi:10.1190/1.1442403, 1988.

Manassero, M. C., Afonso, J. C., Zyserman, F., Zlotnik, S. and Fomin, I.: A reduced order approach for probabilistic inversions of 3-D magnetotelluric data I: general formulation, Geophys. J. Int., 223, 1837–1863, doi:10.1093/gji/ggaa415, 2020.

Martin, R., Monteiller, V., Komatitsch, D., Perrouty, S., Jessell, M., Bonvalot, S. and Lindsay, M. D.: Gravity inversion using wavelet-based compression on parallel hybrid CPU/GPU systems: application to southwest Ghana, Geophys. J. Int., 195, 1594–1619, doi:10.1093/gji/ggt334, 2013.

Moorkamp, M.: Integrating Electromagnetic Data with Other Geophysical Observations for Enhanced Imaging of the Earth: A Tutorial and Review, Surv. Geophys., 1–28, doi:10.1007/s10712-017-9413-7, 2017.

Moorkamp, M.: Joint inversion of gravity and magnetotelluric data from the Ernest-Henry IOCG deposit with a variation of information constraint, in First International Meeting for Applied Geoscience & Energy Expanded Abstracts, pp. 1711–1715, Society of Exploration Geophysicists., 2021.

Moorkamp, M., Heincke, B., Jegen, M., Hobbs, R. W. and Roberts, A. W.: Joint Inversion in Hydrocarbon Exploration, in Integrated Imaging of the Earth: Theory and Applications, pp. 167–189., 2016.

Ogarko, V., Giraud, J., Martin, R. and Jessell, M.: Disjoint interval bound constraints using the alternating direction method of multipliers for geologically constrained inversion: Application to gravity data, GEOPHYSICS, 86, G1–G11, doi:10.1190/geo2019-0633.1, 2021a.

Ogarko, V., Giraud, J. and Martin, R.: Tomofast-x v1.0 source code, , doi:10.5281/zenodo.4454220, 2021b.

Oliver-Ocaño, F. M., Gallardo, L. A., Romo-Jones, J. M. and Pérez-Flores, M. A.: Structure of the Cerro Prieto Pull-apart basin from joint inversion of gravity, magnetic and magnetotelluric data, J. Appl. Geophys., 170, 103835, doi:10.1016/j.jappgeo.2019.103835, 2019.

Paige, C. C. and Saunders, M. A.: LSQR: An Algorithm for Sparse Linear Equations and Sparse Least Squares, ACM Trans. Math. Softw., 8, 43–71, doi:10.1145/355984.355989, 1982.

Pakyuz-Charrier, E., Lindsay, M., Ogarko, V., Giraud, J. and Jessell, M.: Monte Carlo simulation for uncertainty estimation on structural data in implicit 3-D geological modeling, a guide for disturbance distribution selection and parameterization, Solid Earth, 9, 385–402, doi:10.5194/se-9-385-2018, 2018.

Pakyuz-Charrier, E., Jessell, M., Giraud, J., Lindsay, M. and Ogarko, V.: Topological analysis in Monte Carlo simulation for uncertainty propagation, Solid Earth, 10, 1663–1684, doi:10.5194/se-10-1663-2019, 2019.

Pakyuz-Charrier, E. I. G.: Mansfield (Victoria, Australia) area original GeoModeller model and relevant MCUE outputs, , doi:10.5281/zenodo.848225, 2018.

Le Pape, F., Jones, A. G., Jessell, M. W., Perrouty, S., Gallardo, L. A., Baratoux, L., Hogg, C., Siebenaller, L., Touré, A., Ouiya, P. and Boren, G.: Crustal structure of southern Burkina Faso inferred from magnetotelluric, gravity and magnetic data, Precambrian Res., 300, 261–272, doi:10.1016/j.precamres.2017.08.013, 2017.

Ren, Z. and Kalscheuer, T.: Uncertainty and Resolution Analysis of 2D and 3D Inversion Models Computed from Geophysical Electromagnetic Data, Surv. Geophys., doi:10.1007/s10712-019-09567-3, 2019.

Rodi, W. L., Mackie, R. L., Chave, A. D., Jones, A. G., Mackie, R. and Rodi, W.: The inverse problem, in The Magnetotelluric Method, pp. 347–420, Cambridge University Press, Cambridge., 2012.

Scalzo, R., Kohn, D., Olierook, H., Houseman, G., Chandra, R., Girolami, M. and Cripps, S.: Efficiency and robustness in Monte Carlo sampling of 3-D geophysical inversions with Obsidian v0.1.2: Setting up for success, Geosci. Model Dev. Discuss., 1–28, doi:10.5194/gmd-2018-306, 2019.

Schweizer, D., Blum, P. and Butscher, C.: Uncertainty assessment in 3-D geological models of increasing complexity, Solid Earth, 8, 515–530, doi:10.5194/se-8-515-2017, 2017.

Seillé, H. and Giraud, J.: Synthetic dataset for the testing of an MT-Mag geophysical integration workflow, doi: 10.5281/zenodo.5246582 , 2021.

Seillé, H. and Visser, G.: Bayesian inversion of magnetotelluric data considering dimensionality discrepancies, Geophys. J. Int., 223, 1565–1583, doi:10.1093/gji/ggaa391, 2020.

Seillé, H., Visser, G., Markov, J. and Simpson, J.: Probabilistic Cover-Basement Interface Map in Cloncurry, Australia, Using Magnetotelluric Soundings, J. Geophys. Res. Solid Earth, 126, doi:10.1029/2021JB021883, 2021.

Shannon, C. E. E.: A Mathematical Theory of Communication, Bell Syst. Tech. J., 27, 379–423, doi:10.1002/j.1538-7305.1948.tb01338.x, 1948.

Sun, J. and Li, Y.: Multidomain petrophysically constrained inversion and geology differentiation using guided fuzzy c-means clustering, Geophysics, 80, ID1–ID18, doi:10.1190/geo2014-0049.1, 2015.

Tarantola, A.: Inverse Problem Theory and Methods for Model Parameter Estimation, Society for Industrial and Applied Mathematics., 2005.

Tveit, S., Mannseth, T., Park, J., Sauvin, G. and Agersborg, R.: Combining CSEM or gravity inversion with seismic AVO inversion, with application to monitoring of large-scale CO2 injection, Comput. Geosci., 24, 1201–1220, doi:10.1007/s10596-020-09934-9, 2020.

Visser, G.: Smart stitching: adding lateral priors to ensemble inversions as a post-processing step, ASEG Ext. Abstr., 2019, 1–4, doi:10.1080/22020586.2019.12073075, 2019.

Visser, G. and Markov, J.: Cover thickness uncertainty mapping using Bayesian estimate fusion: leveraging domain knowledge, Geophys. J. Int., 219, 1474–1490, doi:10.1093/gji/ggz358, 2019.

Visser, G., Seillé, H. and Markov, J.: Approximating Probabilistic Joint Inversion using Bayesian Spatial Ensemble Fusion, in Proceedings of the EGU General Assembly 2020, pp. EGU2020–4388, European Geophysical Union, Online., 2020.

Wellmann, F. and Caumon, G.: 3-D Structural geological models: Concepts, methods, and uncertainties, edited by C. Schmelzback, pp. 1–121, Cambridge, Massachusetts., 2018.

Wellmann, J. F. and Regenauer-Lieb, K.: Uncertainties have a meaning: Information entropy as a quality measure for 3-D geological models, Tectonophysics, 526–529, 207–216, doi:10.1016/j.tecto.2011.05.001, 2012.

Wilson, G., Čuma, M. and Zhdanov, M. S.: Massively parallel 3D inversion of gravity and gravity gradiometry data, Preview, 2011, 29–34, doi:10.1071/pvv2011n152p29, 2011.

Zhang, R., Li, T., Deng, X., Huang, X. and Pak, Y.: Two-dimensional data-space joint inversion of magnetotelluric, gravity, magnetic and seismic data with cross-gradient constraints, Geophys. Prospect., 68, 721–731, doi:10.1111/1365-2478.12858, 2020.

Appendix A

We reformulate the geophysical inverse problem in eq. (5) in its ADMM form as:

$$\begin{aligned}&\text{minimize } \theta(\boldsymbol{d},\boldsymbol{m}) + f(\boldsymbol{z}) \\ &\quad \text{subject to } \boldsymbol{m} - \boldsymbol{z} = 0,\end{aligned} \tag{15}$$

where f is the indicator function of $\mathcal{B}$ (see eq. 5.1 in Boyd, 2011, for details).We solve this problem iteratively by alternating the updates of $\boldsymbol{m}$ and $\boldsymbol{z}$ following :

$$\boldsymbol{m}^{k+1} = \arg\min_{\boldsymbol{m}}(\theta(\boldsymbol{d},\boldsymbol{m}) + \tau^2 \|\boldsymbol{W_{ADMM}}(\boldsymbol{m} - \boldsymbol{z}^k + \boldsymbol{u}^k)\|_2^2), \tag{16}$$

$$\boldsymbol{z}^{k+1} = \pi_{\mathcal{B}}(\boldsymbol{m}^{k+1} + \boldsymbol{u}^k), \tag{17}$$

$$\boldsymbol{u}^{k+1} = \boldsymbol{u}^k + \boldsymbol{m}^{k+1} - \boldsymbol{z}^{k+1}, \tag{18}$$

where $\boldsymbol{u}$ is called a dual variable, $\tau \in \mathbb{R}^+$ is the overall weight assigned to the ADMM constraints, and k is the current iteration number; $\boldsymbol{W_{ADMM}}$ is a diagonal matrix we introduce here to define spatially varying weights assigned to the bound constraints during inversion. It controls the relative strength of the ADMM constraints in the different model cells. Here, we set it as a function of the MT inversion results $\boldsymbol{P_{MT}}$ such that $\boldsymbol{W_{ADMM}} = \boldsymbol{f}(\boldsymbol{P_{MT}})$. The ADMM variable $\boldsymbol{z}$ is calculated by the projection of $\boldsymbol{x}$ onto $\mathcal{B}$ as:

$$\pi_{\mathcal{B}}(\boldsymbol{x}) = \left[\pi_{\mathcal{B}_1}(x_1), \pi_{\mathcal{B}_2}(x_2), \dots, \pi_{\mathcal{B}_n}(x_n)\right], \text{ with} \tag{19}$$

$$\pi_{\mathcal{B}_i}(x_i) = \arg\min_{y\in\mathcal{B}_i} \|x_i - y\|_2 \tag{20}$$

The updated model $\boldsymbol{m}^{k+1}$ is then calculated by solving the inverse problem using the LSQR algorithm of Paige and Saunders (1982). We refer the reader to Ogarko et al. (2021a) for more details. We illustrate the application of such projection using two intervals in Figure A 1.

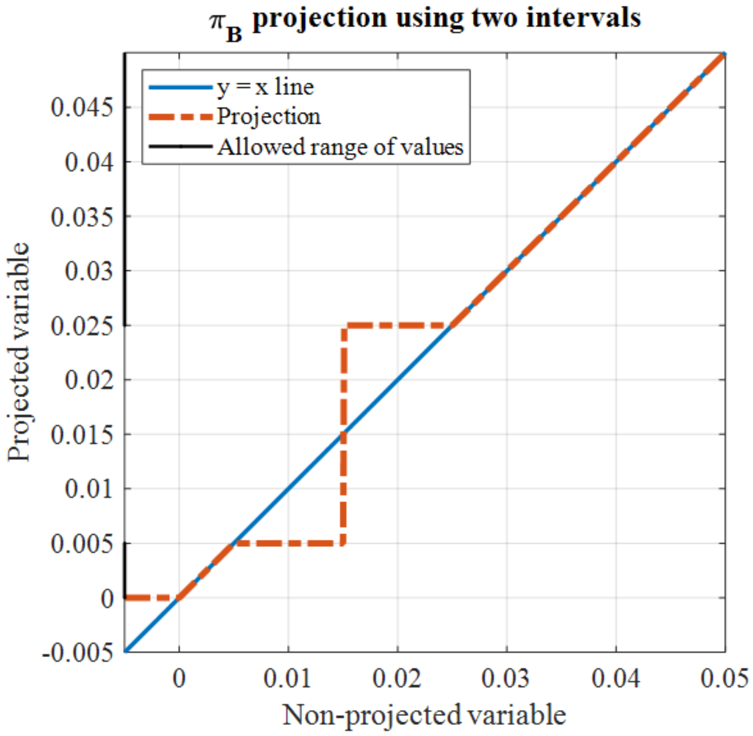

Figure A 1. Projection using $\boldsymbol{\pi_{\mathcal{B}}}$ as per eq. 19 using two intervals as follows: [0, 0.005], [0.025, +∞[. This example uses the intervals selected in the synthetic case study illustrating the proof-of-concept introduced in Sect. 3.